



**HAL**  
open science

# Links Between Faulting, Topography, and Sediment Production During Continental Rifting: Insights From Coupled Surface Process, Thermomechanical Modeling

Lorenz Wolf, Ritske S Huismans, Delphine Rouby, Robert Gawthorpe,  
Sebastian G Wolf

► **To cite this version:**

Lorenz Wolf, Ritske S Huismans, Delphine Rouby, Robert Gawthorpe, Sebastian G Wolf. Links Between Faulting, Topography, and Sediment Production During Continental Rifting: Insights From Coupled Surface Process, Thermomechanical Modeling. *Journal of Geophysical Research : Solid Earth*, 2022, 127 (3), 10.1029/2021JB023490 . insu-03747056v2

**HAL Id: insu-03747056**

**<https://insu.hal.science/insu-03747056v2>**

Submitted on 7 Aug 2022

**HAL** is a multi-disciplinary open access archive for the deposit and dissemination of scientific research documents, whether they are published or not. The documents may come from teaching and research institutions in France or abroad, or from public or private research centers.

L'archive ouverte pluridisciplinaire **HAL**, est destinée au dépôt et à la diffusion de documents scientifiques de niveau recherche, publiés ou non, émanant des établissements d'enseignement et de recherche français ou étrangers, des laboratoires publics ou privés.

1  
2  
3  
4  
5  
6  
7  
8  
9  
10  
11  
12  
13  
14  
15  
16  
17  
18  
19  
20  
21  
22

**Link between faulting, topography, and sediment production during continental rifting: Insights from coupled surface process thermo-mechanical modelling**

List of authors:

Lorenz Wolf<sup>1</sup>, Ritske S. Huismans<sup>1</sup>, Delphine Rouby<sup>2</sup>, Robert Gawthorpe<sup>1</sup>, Sebastian G. Wolf<sup>1</sup>

<sup>1</sup>Department of Earth Science, Bergen University, Bergen N-5007, Norway

<sup>2</sup>Géosciences Environnement Toulouse, UMR5563 CNRS–IRD–Université de Toulouse, 31400 Toulouse, France

Corresponding author: [lorenz.michel@uib.no](mailto:lorenz.michel@uib.no)

**Key Points**

- Coupled, thermo-mechanical models show that during continental rifting, the sediment flux reflects the topographic evolution of rifts.
- High crustal strength, slow extension and efficient surface processes promote strain localization and sediment production.
- Models show that a time-lag of 2 – 5 Myr between the main tectonic activity and the peak in sediment flux could exist for natural systems.

23 **Abstract**

24 Continental rifts form by extension, and their subsequent evolution depends on the tectonic and  
25 climatic boundary conditions. Here, we investigate how faulting, topography, and the evolution of the  
26 sediment flux during rifting are affected by these boundary conditions. In particular, we want to  
27 elucidate whether it is possible to correlate tectonic activity, topography, and sediment flux on long  
28 timescales (40 Myr). We use a thermo-mechanical model coupled with a landscape evolution model  
29 and present a series of 14 models, testing the sensitivity of the models to crustal strength, extension  
30 rate, and fluvial erodibility. The degree of strain localization drives the structural evolution of the  
31 modelled rifts: slow extension, high crustal strength, and efficient surface processes promote a high  
32 degree of strain localization, resulting in less active faults with larger offset on them. Overall, the  
33 magnitude of sediment production correlates with the degree of strain localization. In case of  
34 unchanged erosional power, systems with slower extension produce more sediment owing to a  
35 stronger positive feedback between erosion and fault offset. We observe a characteristic sequence of  
36 events, reflecting the geomorpho-tectonic stages of the rifts: the highest rock uplift rates are observed  
37 before the maximum elevation, and the highest sediment flux postdates the peak in elevation. Our  
38 results indicate that for natural systems, the evolution of the sediment flux is a good proxy for the  
39 evolution of topography, and that a gap of 2 – 5 Myr between the peaks in main tectonic activity and  
40 sediment flux can exist.

41 **Plain Language Summary**

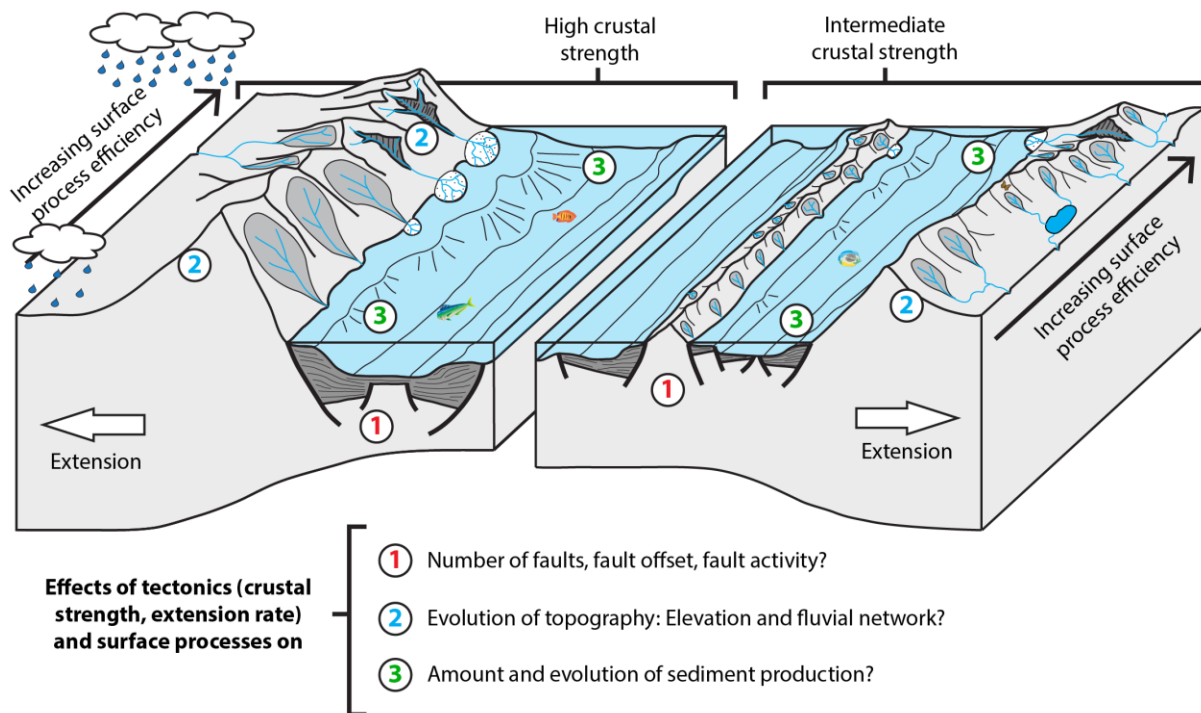
42 Continental rifting is the response of the uppermost part of the Earth to extensional, tectonic forces.  
43 The resulting landscape consists of subsided, sediment-filled basins and uplifted, high-elevation rift  
44 shoulders. Resolving what contributes to rifting on long-timescales (i.e., tens of millions of years)  
45 from natural examples is challenging, since inverting the sedimentary record to resolve correlations  
46 between tectonic activity, topography and the sediment production relies on several assumptions. We  
47 use computer models to simulate continental rifting, and subject the models to different boundary  
48 conditions. This allows us to have a holistic view of the rifting process under variable conditions over  
49 a 40-Million-year period, and we assess how the topography, tectonic deformation and sediment

50 production evolve over time. We see that the degree of localization of deformation is decisive for the  
51 evolution of the rifts, and that localization correlates with sediment production. Furthermore, the  
52 temporal evolution of the sediment production reflects the tectonic and topographic evolution. Moving  
53 from models to natural examples, our findings indicate that the evolution of the sediment production is  
54 a good proxy for topography. However, a gap of 2 – 5 Million years could exist between the main  
55 tectonic activity and the highest sediment production.

56

## 57 **1 Introduction**

58 The Earth's surface is shaped both by tectonic and surface processes. Identifying possible couplings  
59 and feedbacks between tectonic and surface processes has been a focus of research during the past  
60 decades (e.g., Champagnac et al., 2012; Molnar & England, 1990; Whipple, 2009; Whittaker, 2012). A  
61 plethora of studies focused on mountain belts and showed that orographic precipitation can focus  
62 deformation and exhumation (Beaumont et al., 1992; Willett, 1999), that spatial and temporal  
63 variations in uplift and exhumation can be controlled by erosion (e.g., Enkelmann et al., 2009; Grujic  
64 et al., 2006), that variations in erosion reflect variations in tectonically-controlled rock uplift (e.g.,  
65 Adams et al., 2015; Michel et al., 2018; Wang et al., 2014), and how sensitive the orogen-deformation  
66 is to erosion and deposition (Erdős et al., 2015; Wolf et al., 2021). In extensional settings, a high  
67 lithospheric strength increases rift asymmetry and rift shoulder elevation (e.g., Beucher & Huismans,  
68 2020; Corti et al., 2018; Theunissen & Huismans, 2019). Studies documented that a feedback between  
69 footwall erosion and hanging wall deposition leads prolongs fault activity and offset (Maniatis et al.,  
70 2009; Olive et al., 2014), which enhances the formation of large offset asymmetric normal faults  
71 (Beucher & Huismans, 2020; Theunissen & Huismans, 2019), and that enhanced sediment supply to  
72 the rift basin owing to an antecedent river network can localize fault displacement (Hemelsdaël et al.,  
73 2017). All these studies demonstrate, how sensitive the evolution of orogens and rifts is to both  
74 tectonic and climatic boundary conditions.



75

76 **Figure 1: Cartoon illustrating the effects of tectonic and surface processes on the development of rifts.**

77 Tectonically-driven extension leads to uplift and subsidence of the landscape, resulting in rift shoulder uplift and  
 78 basin subsidence. Depending on the crustal strength (left or right part of the cartoon), the resulting rift  
 79 geometries can be different. Surface processes such as fluvial erosion or hillslope processes lower the elevated  
 80 landscape and generate sediment. The efficiency of the surface processes affects the topography and the  
 81 deposition of sediments in the basins (erosion increases from the front towards the back of the cartoon). The  
 82 numbers indicate specific questions that are addressed in this work, and that are related to the effects of the  
 83 tectonic (extension rate, crustal strength) and climatic boundary conditions (efficiency of surface processes).  
 84 Modified from Whittaker et al. (2010).

85

86 At continental rifts, tectonically driven faulting leads to uplift and subsidence of the landscape,  
 87 forming rifts with high-elevation shoulders and bounding basins (Fig. 1). Climatically influenced  
 88 surface processes erode the landscape, create relief and produce sediments that infill the tectonically  
 89 generated depressions creating the stratigraphic record of a basin (Fig. 1). Variations in the associated  
 90 sediment flux can be related both to tectonic and climatic causes (e.g., Forzoni et al., 2014; McNeill et  
 91 al., 2019; Rohais & Rouby, 2020; Sømme et al., 2019) and in turn, the preserved stratigraphic record is  
 92 often used to unravel the effects of tectonic or surface processes, for instance by inferring the history  
 93 of rock uplift, the evolution of topography and the drainage network, and climatic variations (e.g.,

94 Armitage et al., 2011; Castellort & Van Den Driessche, 2003; Geurts et al., 2020; Guillocheau et al.,  
95 2012; Rohais & Rouby, 2020; Sømme et al., 2019; Stevens Goddard et al., 2020; Whittaker et al.,  
96 2010). Correlations between catchment area, runoff, relief, and sediment flux observed in present-day  
97 river systems (Syvitski & Milliman, 2007) are commonly used to invert the evolution of the sediment  
98 flux (as preserved in the stratigraphic record) for instance for the evolution of past relief and  
99 catchment area (e.g., Rohais & Rouby, 2020; Sømme et al., 2019). One of the inherent assumptions for  
100 this approach is that temporal variations in the sediment flux are coeval and correlated with changes in  
101 relief or catchment area also on long timescales a (e.g., as induced by tectonically-controlled changes  
102 in rock uplift). However, obtaining independent constraints on past topographic evolution and linking  
103 this to sediment flux is challenging.

104         The simple correlation between tectonic activity, topography, and sediment flux on geologic  
105 timescales implicit in the BQART method is, furthermore, hampered by the transient response of  
106 landscapes to changes in tectonic and/or climatic conditions, and by possible feedbacks between  
107 tectonic and surface processes (e.g., Allen, 2008; Allen & Heller, 2011; Li et al., 2018; Whittaker et  
108 al., 2010). Here, we aim to circumvent these limitations and obtain coeval constraints on topography,  
109 tectonic activity, and sediment production using coupled forward modelling. We analyse the evolution  
110 of continental rifts from the syn-rift to the post-rift using a high-resolution 2D thermo-mechanical  
111 model coupled with a landscape evolution model, and subject the rifts to different tectonic and surface  
112 process boundary conditions. The landscape evolution model includes the temporally and spatially  
113 transient uplift field of faults and simulates the erosional response of the evolving landscape. In turn,  
114 the tectonic model includes the effects of erosion and deposition on the evolution of lithosphere  
115 deformation and fault formation. Hence, the model allows investigating the response of tectonics (i.e.,  
116 evolution of the structure of a rift, number of faults, fault offset) to the redistribution of mass by  
117 erosion and sedimentation, and at the same time allows measuring the amount of sediment generated  
118 over time. We address the following questions (Fig. 1): (1) What is the influence of different boundary  
119 conditions, specifically crustal strength, erosional power, and extension rate on the structural and  
120 topographic evolution of rifts? (2) How do the boundary conditions affect sediment production? (3)

121 How are the evolution of sediment flux, topography, and tectonic activity correlated on long  
122 timescales?

123 The response of sediment production to variations in tectonic and climatic boundary  
124 conditions has been the subject of previous work using surface process models (e.g., Armitage et al.,  
125 2011; Densmore et al., 2007; Forzoni et al., 2014; Li et al., 2018; Yuan et al., 2019). These models  
126 used either simple 1D geometries or were restricted to a limited-spatial extent (i.e., focusing on a  
127 single catchment), considered only short timescales (< 15 Myr), or simplified the tectonics using  
128 uniform uplift fields. Inherent to all of these studies is that they are not able to include the effect of  
129 erosion and deposition on fault offset owing to their lacking mechanical part. On the other hand,  
130 previous work using coupled models in rift settings often used simple tectonic boundary conditions  
131 and focused for instance solely on the role of the crustal rheology using fixed extension rates (e.g.,  
132 Andrés-Martínez et al., 2019; Beucher & Huismans, 2020; Olive et al., 2014; Theunissen & Huismans,  
133 2019). These studies demonstrated that rheology affects the coupling between crust and mantle  
134 (Beucher & Huismans, 2020; Huismans & Beaumont, 2002, 2003; Theunissen & Huismans, 2019)  
135 and showed a feedback between erosion, hanging wall deposition, and fault offset (Andrés-Martínez et  
136 al., 2019; Olive et al., 2014; Theunissen & Huismans, 2019). Other work using purely thermo-  
137 mechanical models also highlighted the effect of extension rate on the width, asymmetry, and  
138 distribution of deformation of rifts and rifted margins (Huismans & Beaumont, 2002, 2003; Naliboff et  
139 al., 2017; Svartman Dias et al., 2015; Tetreault & Buitert, 2018). We build upon these conclusions and  
140 as tectonic boundary conditions, we test the sensitivity of the models to both variable crustal  
141 rheologies and different extension rates. In order to test the sensitivity of the models to surface  
142 processes, we vary the erodibility between the models.

143 We present a series of 14 numerical experiments, where we systematically vary the tectonic  
144 and surface process efficiency parameters. We focus on elucidating changes in the sediment  
145 production both during the syn-rift and post-rift phase and on what the underlying mechanisms are.  
146 We analyse (1) the structural and topographic evolution of the rifts and (2) how this impacts the  
147 evolution of the sediment flux. For selected models, we provide detailed analyses of fault activity,

148 fault offset, and topography. Furthermore, we relate the temporal evolution of the sediment flux with  
149 the temporal evolution of elevation and rock uplift, identifying four phases that reflect the geomorpho-  
150 tectonic evolution of the rift. We also discuss, where they can be observed in natural examples. We  
151 finally assess, how our model results corroborate the approach to invert the sediment record for the  
152 topographic evolution of rifts.

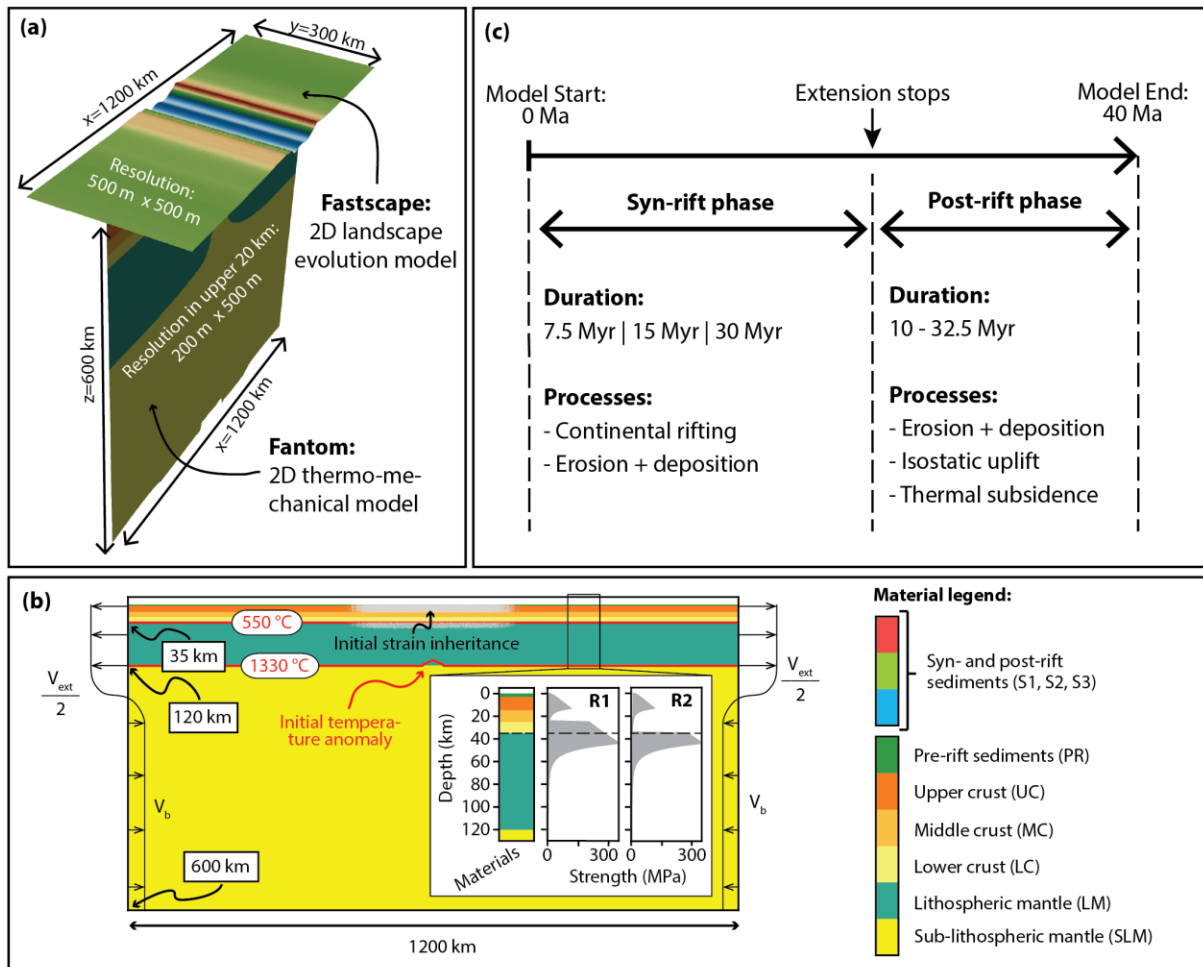
## 153 **2 Modelling Methods**

### 154 **2.1 The T-model: a coupled thermo-mechanical-surface-process model**

155 We use a lithosphere-scale thermo-mechanical-surface-process model to investigate continental rifting  
156 (Wolf et al. 2021; see Fig. 2a). The model consists of the 2D thermo-mechanical code Fantom  
157 (Thieulot, 2011), coupled to the 2D landscape evolution code FastScape (Braun & Willett, 2013; Yuan  
158 et al., 2019). FastScape and Fantom are tightly coupled in a T-manner (Beaumont et al., 1992; Wolf et  
159 al., 2021), so that uplift and subsidence arising from the thermo-mechanical model provide a  
160 cylindrical uplift signal to FastScape and average erosion and deposition feed back to the thermo-  
161 mechanical computation. The coupled model captures the temporally and spatially transient evolution  
162 of continental rifts subject to the interaction between surface processes and tectonics. In the following,  
163 we describe the setup and boundary conditions of the tectonic and surface process model and explain  
164 the strategy behind our modelling approach.

### 165 **2.2 Setup and boundary conditions for Fantom**

166 Fantom is a thermo-mechanically coupled, arbitrary Lagrangian-Eulerian, finite-element code that  
167 solves for plane-strain, incompressible, visco-plastic creeping flows and heat transfer in the model  
168 domain. Viscous deformation is approximated by nonlinear power law creep and material properties  
169 are based on flow laws of wet quartz (Gleason & Tullis, 1995), dry Maryland diabase (Mackwell et al.,  
170 1998) and wet olivine (Karato & Wu, 1993). Frictional-plastic deformation is modelled using a  
171 pressure-dependent Drucker-Prager yield criterion, considering the effect of plastic strain-weakening  
172 on the materials (Huisman & Beaumont, 2003). A full explanation of the inherent equations and a  
173 table of all material constants is given in the electronic supplement (section S1 and Table S1).



174

175 **Figure 2: Model setup** (a) Overview, model dimensions, and resolutions of the T-model, where a 2D landscape  
 176 evolution model (FastScape) is coupled with a 2D thermo-mechanical model (Fantom). (b) Model setup and  
 177 geometry for Fantom, illustrating the layered structure (all thermal and mechanical properties are summarized in  
 178 Table S1 in the supplement), the boundary conditions ( $V_{\text{ext}}$  = extension rate,  $V_b$  = velocity of basal counter flow)  
 179 and the initial thermal state (red lines). Location and extent of features that promote strain localization at the  
 180 beginning of extension are indicated: initial temperature anomaly (notch in the 1330°C isotherm) and strain  
 181 inheritance. The inset displays a close-up view of the upper 130 km of the model, and the strength envelopes of  
 182 the two different rheologies considered in our models, which differ in the strength of the lower crust (R1 = high  
 183 crustal strength, R2 = intermediate crustal strength). (c) Temporal evolution of the models: The models have a  
 184 total duration of 40 Myr and syn-rift duration depends on the extension rate (7.5 Myr, 15 Myr, 30 Myr).

185

186 The model domain is 1200 km wide, 600 km deep, and vertically stratified (Fig. 2b). From top  
 187 to bottom the model consists of continental crust (0–35 km), lithospheric mantle (35–120 km), and  
 188 sub-lithospheric mantle (120–600 km). To test the sensitivity of the model to different crustal  
 189 strengths, we discern two different crusts, R1, strong crust, and R2, intermediate strength crust (see

190 strength envelopes in the inset of Fig. 2b). R1 uses dry Maryland diabase as material for the lower  
191 crust, R2 uses wet quartz for the lower crust. Otherwise, the two rheologies consist of the same  
192 materials, using wet quartz as material for the upper parts of the crust and wet olivine for the  
193 lithospheric and sublithospheric mantle. To account for stronger, melt-depleted conditions, the flow  
194 law of the lithospheric mantle is scaled by a factor 5. We do not consider models with an even weaker  
195 crust (see for instance, Huisman & Beaumont, 2011; Theunissen & Huisman, 2019), because very  
196 weak crust does not result in significant rift initialization for the extension durations that we consider.  
197 Material that is eroded and deposited as sediment during the model run (materials S1, S2 and S3 in  
198 Fig. 2b) has the same mechanical properties as upper crust.

199 We use a 400 km wide area in the centre of the model with initial strain inheritance (Fig. 2b),  
200 simulating inherited structures from previous tectonic events (Theunissen & Huisman, 2019). To  
201 localize rifting in the centre of this domain, we add a small thermal anomaly at the base of the  
202 lithosphere in the centre of the model (Fig. 2b). A more detailed explanation of the approach for strain  
203 inheritance can be found in the electronic supplement.

204 On each side of the model, the lithosphere is extended with half the extension rate as  
205 horizontal velocity boundary condition ( $v_{\text{ext}}$  in Fig. 2b). Lateral outflow of material is balanced by a  
206 low velocity inflow of material in the sub-lithospheric mantle in order to preserve mass ( $v_b$  in Fig. 2b).  
207 The bottom and sides of the model are horizontal and vertical free slip boundaries, respectively,  
208 whereas the top of the model serves as free surface subject to erosion and deposition. As thermal  
209 boundary condition the base of the model is kept at a constant temperature of 1522 °C and the lateral  
210 boundaries are thermally insulated. The numerical resolution in our models is 500 m horizontally and  
211 the vertical resolution is depth dependent with a 200 m resolution in the upper 20 km. This high  
212 resolution allows investigating the basin-scale feedback of tectonics and surface processes.

### 213 **2.3 Setup and boundary conditions for FastScape**

214 We use a modified version of FastScape to model surface processes (Braun & Willett, 2013; Yuan et  
215 al., 2019). FastScape accounts for onshore erosion, sediment transport, and deposition in the marine  
216 part of the landscape. The rate of change of elevation ( $\partial h/\partial t$ ) in the parts of the landscape above sea

217 level is simulated by solving the stream power law (i.e., river incision; Whipple & Tucker, 1999), and  
218 hillslope processes (Culling, 1963):

$$219 \quad \frac{\partial h}{\partial t} = U - k_f A^m S^n + k_C \nabla^2 h, \quad \text{for } h \geq h_{\text{sea level}} \quad (1)$$

220 where  $h$  is elevation,  $U$  is uplift rate,  $k_f$  is fluvial erodibility,  $A$  is upstream drainage area,  $S$  is slope,  $m$   
221 and  $n$  are stream power law exponents, and  $k_C$  is the transport coefficient of hillslope diffusion. We do  
222 not include continental deposition. Hence, no material is deposited above sea level and all eroded  
223 material is transported by the rivers to the marine domain or out of the model according to the  
224 drainage organisation.

225 Below sea level, sediment transport and deposition are simulated using a diffusion equation as  
226 described in Yuan et al. (2019). Using the amount of sediment flux coming from the continental  
227 domain of the model ( $Q_s$ ), the rate of elevation change can be approximated by:

$$228 \quad \frac{\partial h}{\partial t} = k_M \nabla^2 h + Q_s, \quad \text{for } h < h_{\text{sea level}} \quad (3)$$

229 where  $k_M$  is the marine diffusion coefficient. Equation (3) is valid if the material transported below  
230 consists of one grainsize. In our case we consider two different grainsizes and use a coupled-diffusion  
231 with distinct transport coefficients for the two grainsizes (having values of 200 m<sup>2</sup>/yr and 100 m<sup>2</sup>/yr,  
232 respectively). We refer to the paper of Yuan et al. (2019) for further technical details about this  
233 approach.

234 FastScape truly sits on top of Fantom and has the same spatial dimension of 500 m. We  
235 choose a model depth of 400 km for the FastScape model, resembling a typical width of a continental  
236 rift system. The left and right-side boundaries of the landscape are open so that water flows out and the  
237 top and bottom boundaries are periodic.

## 238 **2.4 Modelling strategy**

239 To investigate the variability of tectonic and surface processes in continental rifts, we test the  
240 sensitivity of our models to crustal rheology, extension rate, and fluvial erodibility. The resulting  
241 parameter combinations yield 14 different models (Table 1).

Model name	Rheology	Extension rate [km/Myr]	$K_f$ value [ $\text{m}^{0.2}/\text{yr}$ ]	Evolution displayed in
M1	R1	10	$0.5 \times 10^{-5}$	Fig. 3 Animation 1
M2	R1	5	$0.5 \times 10^{-5}$	Fig. 4 Animation 2
M3	R2	10	$0.5 \times 10^{-5}$	Fig. 5 Animation 3
M4	R1	5	$0.25 \times 10^{-5}$	Fig. 6 Animation 4
M5	R1	5	$1.0 \times 10^{-5}$	Fig. 6 Animation 5
SM1	R1	2.5	$0.5 \times 10^{-5}$	Animation 6
SM2	R2	2.5	$0.5 \times 10^{-5}$	Animation 7
SM3	R1	5	$0.1 \times 10^{-5}$	Animation 8
SM4	R2	5	$0.1 \times 10^{-5}$	Animation 9
SM5	R2	5	$0.25 \times 10^{-5}$	Animation 10
SM6	R2	5	$0.5 \times 10^{-5}$	Animation 11
SM7	R2	5	$1.0 \times 10^{-5}$	Animation 12
SM8	R1	10	$0.25 \times 10^{-5}$	Animation 13
SM9	R1	10	$1.0 \times 10^{-5}$	Animation 14

242 **Table 1:** Summary of parameters of the 14 models with varying tectonic parameters (rheology, extension rate)  
243 and erodibility ( $k_f$  value). R1 refers to strong crust, R2 to intermediate strength crust, see also Fig. 2b. Detailed  
244 analyses of the evolution of structures and topography for the main models (M1 – M5) are provided in Figs. 3 –  
245 6.

246

247 We consider two different crustal rheologies (R1 and R2; Fig. 2b) with a total 75 km of  
248 extension. This is sufficient to develop a rift without reaching crustal breakup. The duration of  
249 extension depends on the extension rate and we consider four combinations of extension rate and  
250 duration: 7.5 Myr at a rate of 10 km/Myr, 15 Myr at a rate of 5 km/Myr, and 30 Myr at a rate of 2.5  
251 km/Myr. All models have a total duration of 40 Myr with variable durations of the syn- and post-rift  
252 phases (Fig. 2c).

253 Fluvial incision controls the erosional efficiency, erosion rate, and sediment yield. In the Stream  
254 Power Law, coefficients  $m$  and  $n$  are relatively well known (Stock & Montgomery, 1999), but fluvial  
255 erodibility ( $k_f$ ) spans a wide range as it incorporates effects related to climate, rock type, vegetation,  
256 and abrasive agents (Stock & Montgomery, 1999). We keep  $m=0.4$  and  $n=1$  and test the effect of  
257 erosional efficiency by changing fluvial erodibility, considering  $k_f$  values of 0.1, 0.25, 0.5 and  $1 \times 10^{-5}$   
258  $\text{m}^{0.2}/\text{yr}$  (Table 1). These values cover a wide range, leading to very little erosion and a long-lasting  
259 landscape or very efficient erosion and rapid degradation of the landscape. This can be envisioned as  
260 rifts experiencing arid to humid climatic boundary conditions. We use a reference  $k_f$  value of  $0.5 \times$   
261  $10^{-5} \text{m}^{0.2}/\text{yr}$  for all of our extension rates and rheologies (Table 1). To account for pre-existing relief,  
262 we set the sea level to -1000 m below the initial model surface (which is at 0 m).

263 We analyse the output from both the tectonic and surface processes models (see electronic  
264 supplement, section S4 for details of analyses procedure). We focus on five models (models M1 – M5  
265 in Table 1), for which we provide detailed analyses of the structural and topographic evolution (Figs. 3  
266 – 6). Supplementary models (SM1 – SM9) are included in the analyses of the evolution of topography  
267 and sediment flux (Figs. 7 – 9). For all models we provide animations of topography and structures in  
268 the electronic supplement.

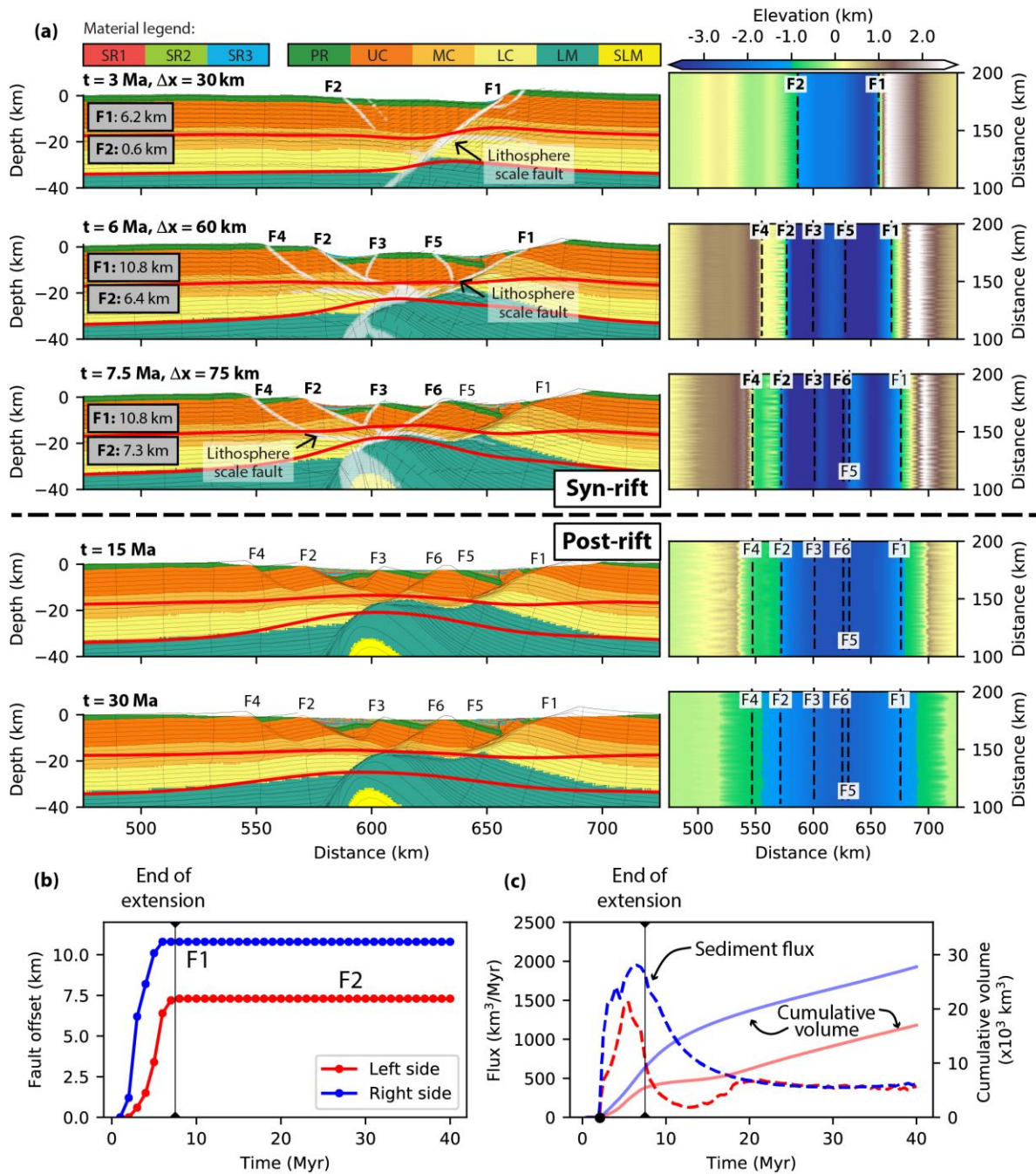
### 269 **3 Results**

270 We provide a detailed description of the evolution of the rift geometry for selected models (M1 – M5,  
271 Table 1). We focus on the reference model M1 and highlight changes in the evolution of rifting. We  
272 then describe the sensitivity of the evolution of elevation and sediment production to extension rate  
273 and erodibility.

#### 274 **3.1 Evolution of rift geometry and faults**

##### 275 **3.1.1 Reference model M1**

276 The reference model has a high crustal-strength (rheology R1; Fig. 2b), intermediate  
277 erodibility ( $k_f = 0.5 \times 10^{-5} \text{m}^{0.2}/\text{yr}$ ), and an extension rate of 10 km/Myr for 7.5 Myr.



278

279 **Figure 3: Results of the reference model M1.** Model results for model M1 with high crustal strength, 7.5 Myr  
 280 of extension (extension rate of 10 km/Myr) and intermediate erodibility ( $k_f = 0.5 \times 10^{-5} \text{ m}^{0.2}/\text{yr}$ ): (a) Structures  
 281 (left column) and topography (right column) at selected time steps. Major faults are labelled in accordance with  
 282 their onset of activity (faults active during the respective timestep are labelled in bold). Numbers in the grey  
 283 boxes indicate vertical fault offset on the two boundary faults (F1 and F2). The black arrows indicate  
 284 lithosphere-scale faults that reach a depth over 15 km. The topography transitions from onshore to offshore at the  
 285 sea level (-1000 m). (b) Evolution of the vertical fault offset on the two boundary faults F1 (blue, right side) and  
 286 F2 (red, left side). (c) Evolution of incremental (dashed curves) and cumulative (solid curves) sediment volumes  
 287 from the two rift sides over time (blue = right side, red = left side).

288           At 3 Ma two boundary faults (F1 and F2) form a 75 km wide asymmetric rift system (Fig. 3a).  
289 Major fault F1 forms a crustal scale shear-zone cutting into the upper mantle lithosphere (Fig. 3a) and  
290 is associated with significant rift shoulder elevation, ~ 3000 m (Fig. 3b). Fault F2 exhibits only ~6 km  
291 displacement and is associated with more subdued topography (Fig. 3a). On both sides of the rift  
292 minor fluvial valleys orthogonal to the main drainage divides form.

293           At 6 Ma, displacement along F1 and F2 reaches 10.8 and 6.4 km respectively (Figs. 3a and  
294 3b), new fault F4 dissects the footwall of F2, and deformation shifts to the centre of the rift forming  
295 faults F3 and F5 (Fig. 3a). Footwall uplift of F4 on the left side reduces the area draining towards the  
296 rift basin. Erosion of the right rift flank is associated with headward migration of the drainage divide.  
297 Material eroded from both rift flanks is deposited in the hanging wall grabens of F1 and F2. Activity  
298 of F1 ceases at 6.5 Ma with a total offset of 10.8 km, while F2 remains active until 7.5 Ma with a total  
299 offset of 7.3 km (Fig. 3b).

300           At 7.5 Ma deformation is partitioned between left flank faults F2 and F4 and the centre of the  
301 rift F3 and F6 (Fig. 3a). The final rift geometry is asymmetric with the highest offset and topography  
302 associated with F1 on the right side (Fig. 3a). On the left side, rift topography is associated with F4,  
303 while the fault block between F2 and F4 forms a low-lying fluvial floodplain next to the basin (Fig.  
304 3a).

305           At 15 Ma both rift flanks are significantly eroded down to ~1 km elevation (Fig. 3a).  
306 Landward drainage divide retreat forms wide low-lying floodplains allowing transit of sediments to  
307 the basin that first fill up the rift bounding half grabens and then the central part of the basin (Fig. 3a).  
308 At 30 Ma, onshore rift flank morphology has been further warped down, and the lateral floodplains  
309 and the central basin are submerged (Fig. 3a).

310           Sediment flux varies strongly throughout the model evolution (Fig. 3c). On the right side of  
311 the rift sediment flux reaches a maximum value of 2000 km<sup>3</sup>/Myr around the end of activity of F1 at  
312 ~6.5 Ma (Fig. 3c) and then decreases exponentially to a steady value at 25 Ma (Fig. 3c). On the left  
313 rift side, the sediment flux peaks earlier and at a lower value ~1500 km<sup>3</sup>/Myr and then similarly

314 decreases exponentially during the post rift. The contrasting evolution of sediment flux through time is  
315 also reflected in the cumulative sediment volumes,  $17 \times 10^3 \text{ km}^3$  and  $28 \times 10^3 \text{ km}^3$  at 40 Ma for the left  
316 and right side, respectively (Fig. 3c).

### 317 **3.1.2 Effect of decreasing extension rate**

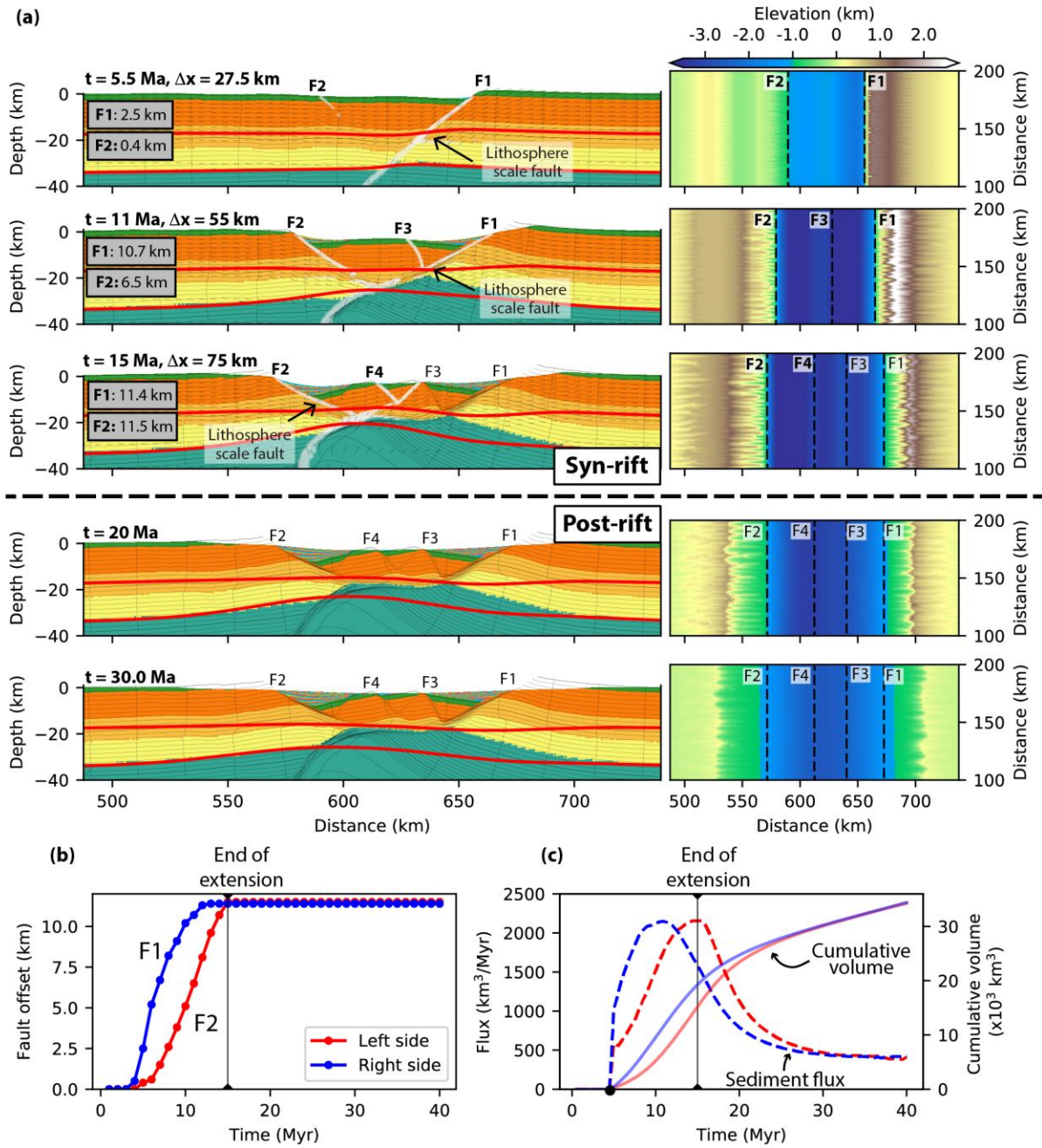
318 Model M2 (Fig. 4) uses half the extension rate of the reference model (5 km/Myr until 15 Ma)  
319 and identical other parameters (high crustal-strength rheology R1, intermediate erodibility  $k_f = 0.5 \times$   
320  $10^{-5} \text{ m}^{0.2}/\text{yr}$ ). Slower extension in M2 delays localization of deformation and rift formation with  
321 respect to reference model M1.

322 At 5.5 Ma, an asymmetric rift has developed with 2.5 km of offset on right boundary rift fault F1 and  
323 rift flank elevation of  $\sim 1500$  m and insipient fault F2 on the left side (Figs. 3a and 3b). With ongoing  
324 extension both F1 and F2 take up most of the deformation leading to a largely symmetric rift at 11 Ma.  
325 Activity on F1 ceases around  $\sim 13.5$  Ma, whereas F2 remains active until the end of extension at 15  
326 Ma. Subsequently, deformation shifts basin-ward breaking up the central block between F1 and F2,  
327 forming conjugate faults F3 and F4 in the centre. In contrast to model M1 most of the deformation is  
328 accommodated by the rift boundary faults F1 and F2 with a similar total offset ( $\sim 11.5$  km) at the end  
329 of extension (Figs. 4b). Sediment flux peaks are similar in magnitude on both sides of the rift and  
330 coincide with the timing of cessation of activity on F1 and F2 (Fig. 4c). Cumulative sediment volume  
331 at 40 Ma is higher than in model M1 reaching the same magnitude on both rift sides (Fig. 4c).

### 332 **3.1.3 Effect of decreasing crustal strength**

333 Model M3 (Fig. 5) investigates the influence of intermediate crustal strength (rheology R2),  
334 lower than in the reference model, with the same extension rate (10 km/Myr), and erodibility ( $k_f = 0.5$   
335  $\times 10^{-5} \text{ m}^{0.2}/\text{yr}$ ).

336 Intermediate crustal strength results in a significantly different rift style compared to models  
337 M1 and M2, with more distributed deformation. At 4 Ma and 40 km extension, a broad 150 km wide,  
338 symmetric graben has formed with equal offset on main rift boundary faults F1 and F2, and secondary  
339 hanging wall faults F3 and F4 (Fig. 5a). Offset along F1 and F2 leads to a maximum rift flank



340

341 **Figure 4: Effect of decreasing the extension rate.** Results for model M2 with high crustal strength, 15 Myr of  
 342 extension (extension rate of 5 km/Myr) and intermediate erodibility ( $k_f = 0.5 \times 10^{-5} \text{ m}^{0.2}/\text{yr}$ ): (a) Structures (left  
 343 column) and topography (right column) at selected time steps. Major faults are indicated and labelled in  
 344 accordance with their onset of activity (faults active during the respective timestep are labelled in bold).  
 345 Numbers in the grey boxes indicate vertical fault offset on the two boundary faults (F1 and F2). The black  
 346 arrows indicate lithosphere-scale faults that reach a great depth ( $>15 \text{ km}$ ). The topography transitions from  
 347 onshore to offshore at the sea level (-1000 m). (b) Evolution of the vertical fault offset on the two boundary  
 348 faults F1 (blue, right side) and F2 (red, left side). (c) Evolution of incremental (dashed curves) and cumulative  
 349 (solid curves) sediment volumes from the two rift sides over time (blue = right side, red = left side).

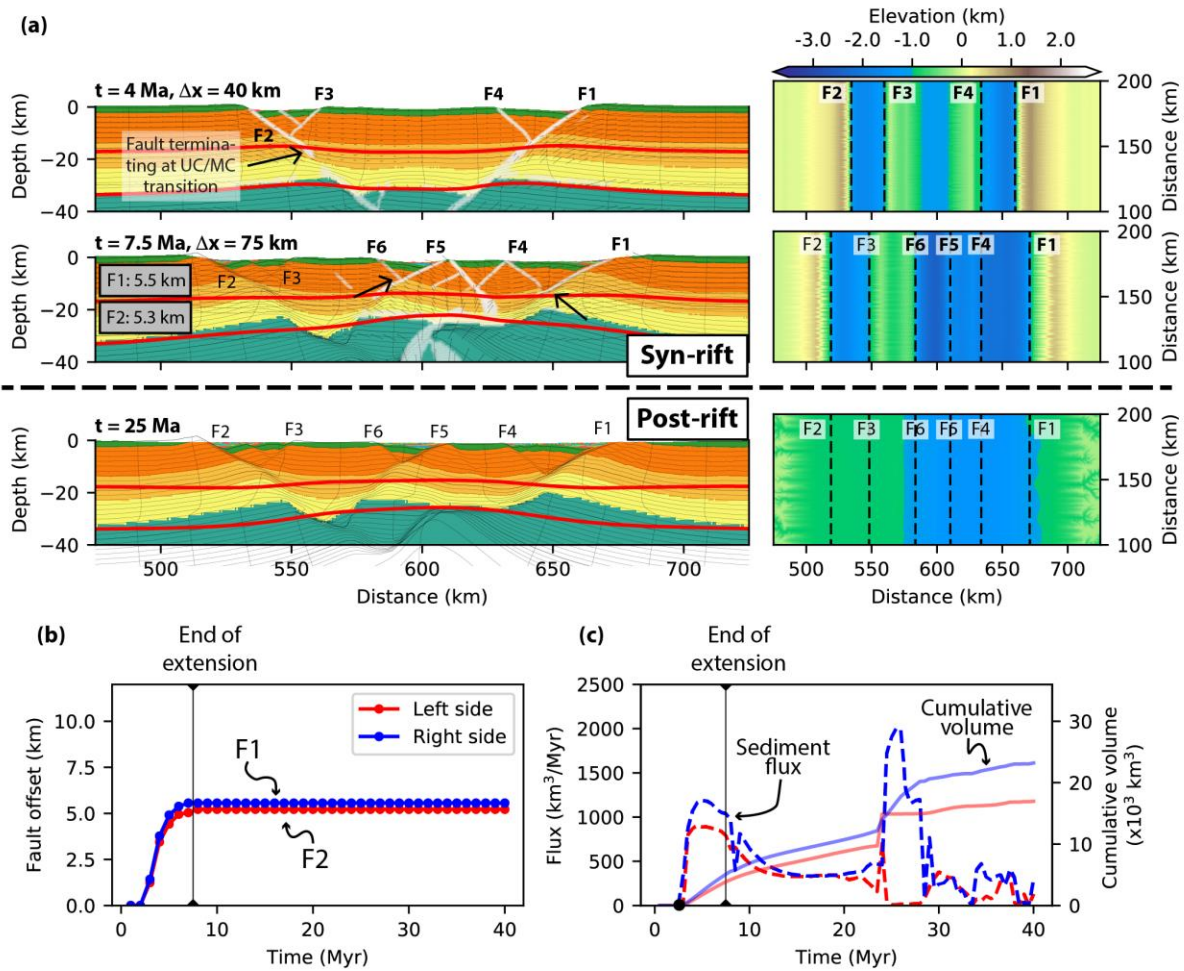
350 elevation of ~1500 m, lower compared to models with strong crustal rheology. Moderate footwall  
351 uplift along secondary hanging wall faults F3 and F4 divides the graben into 3 sub-basins. At 7.5 Ma  
352 major bounding faults F1 and F2 accommodate offsets ~5.5 km, significantly less compared to models  
353 1 and 2 (Fig. 5a). At this stage deformation has migrated to the right half graben breaking up its  
354 hanging wall forming second-generation normal faults F4, F5, and F6 resulting in a broad about 3000  
355 m deep submerged basin. Hanging wall subsidence associated with F2 results in a separate shallow  
356 submerged basin. Post-rift erosion efficiently removes the rift shoulders leading to head-ward erosion,  
357 drainage divide migration, and river capture events around 25 Ma (Fig. 5a). Sediments are deposited in  
358 the half-grabens associated with F1, F2, and F5 leading to rapid infill and a shallow basin at the end of  
359 the model at 40 Ma.

360 Sediment flux (Fig. 5c) varies strongly throughout the model evolution. Peaks from both the  
361 left ( $900 \text{ km}^3$ ) and right ( $1250 \text{ km}^3$ ) side occur at ~6 Ma, coeval with the end of main activity on F2  
362 and F1, respectively (Fig. 5b). On the right rift side, a significant peak in sediment flux (~ $2000 \text{ km}^3$ )  
363 during the post-rift is observed at 25 Ma, related to river capture on the right rift side. The horst  
364 uplifted between F3 and F6 (Fig. 5a) forms a transient, topographic barrier. This prevents the sediment  
365 coming from the left rift side from reaching the central basin, resulting in decreased sediment flux  
366 from the left rift side during 25 – 30 Ma, also reflected in the difference of the cumulative volume of  
367  $12 \times 10^3 \text{ km}^3$  and  $22 \times 10^3 \text{ km}^3$  for the left and right side, respectively.

#### 368 **3.1.4 Effect of erodibility**

369 Models M4, M2, and M5 (Table 1) explore the sensitivity to changing erodibility with  $k_f$  values 0.25,  
370 0.5, and  $1 \times 10^{-5} \text{ m}^{0.2}/\text{yr}$ , respectively. They have a high crustal-strength rheology R1 and a low  
371 extension rate 5 km/Myr. We compare the models at the end of extension at 15 Ma (e.g., Fig. 6; see  
372 supplementary animations for full model evolution).

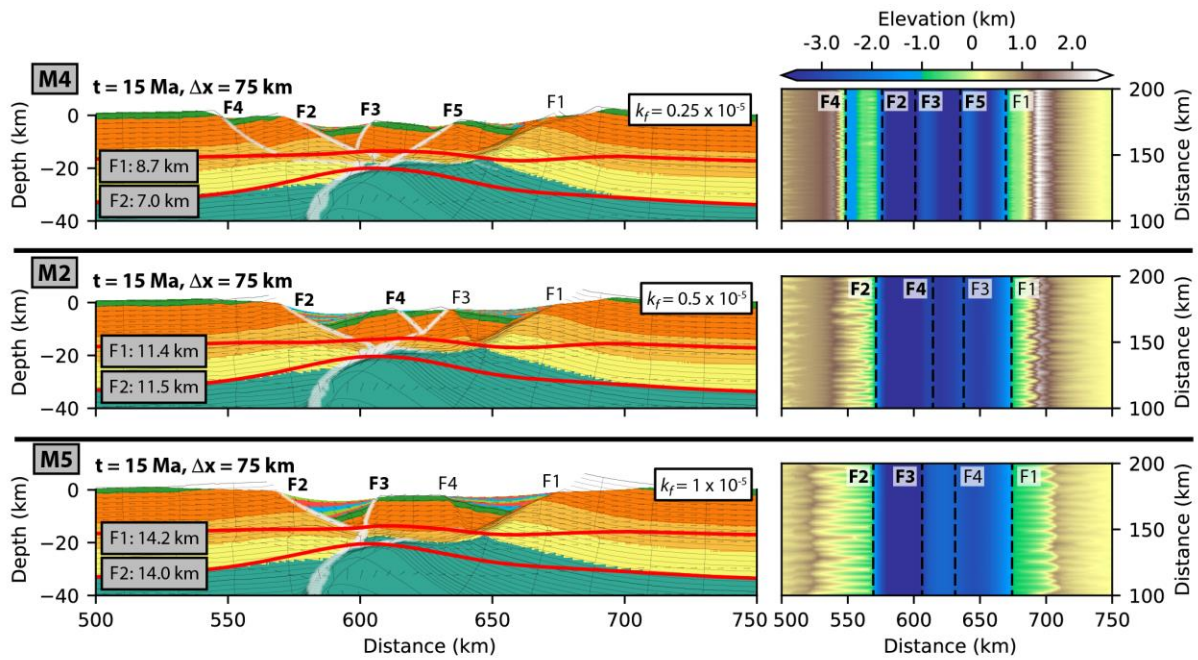
373 Varying erodibility affects both the number and the offset of faults. Model M4 with very low  
374 erodibility exhibits five faults and minor rift flank erosion. In contrast model M2 with intermediate  
375 erodibility is dominated by two main rift boundary faults and moderate rift flank erosion. Model M5  
376 with even higher erodibility shows strongly enhanced offset along F1 and F2 (>14 km), significant rift



377

378 **Figure 5: Effect of decreasing crustal strength.** Results for model M3 with intermediate crustal strength, 7.5  
 379 Myr of extension (extension rate of 10 km/Myr) and intermediate erodibility ( $k_f = 0.5 \times 10^{-5} \text{ m}^{0.2}/\text{yr}$ ): (a)  
 380 Structures (left column) and topography (right column) at selected time steps. Major faults are indicated and  
 381 labelled in accordance with their onset of activity (faults active during the respective timestep are labelled in  
 382 bold). Numbers in the grey boxes indicate vertical fault offset on the two boundary faults (F1 and F2). The black  
 383 arrows indicate faults that terminate at the transition from upper (UC) to middle crust (MC). The topography  
 384 transitions from onshore to offshore at the sea level (which is at -1000 m). (b) Evolution of the vertical fault  
 385 offset on the two boundary faults F1 (blue, right side) and F2 (red, left side). (c) Evolution of incremental  
 386 (dashed curves) and cumulative (solid curves) sediment volumes from the two rift sides over time (blue = right  
 387 side, red = left side).

388



389

390 **Figure 6: Sensitivity to erodibility.** Structures (left column) and topography (right column) at the end of  
 391 extension at 15 Ma for models M2, M4, and M5 with high crustal strength, 15 Myr of extension and variable  
 392 erosional efficiency: (a) M4 with  $k_f = 0.25 \times 10^{-5} \text{ m}^{0.2}/\text{yr}$ , (b) M2 with  $k_f = 0.5 \times 10^{-5} \text{ m}^{0.2}/\text{yr}$ , and (c) M5 with  $k_f$   
 393  $= 1 \times 10^{-5} \text{ m}^{0.2}/\text{yr}$ . Faults are labelled according to their onset of activity, and active faults at 15 Ma are labelled  
 394 in bold. Numbers in the grey boxes indicate vertical fault offset on the two boundary faults (F1 and F2). The  
 395 topography transitions from onshore to offshore at the sea level (-1000 m).

396

397 flank erosion, and thick, tilted sediment wedges.

398 Erodibility also strongly impacts the topography through the drainage system. Low erodibility  
 399 model M4 develops numerous small catchments with a drainage divide at  $\sim 30$  km from the shoreline,  
 400 whereas the high erodibility model M5 develops fewer larger catchments and a drainage divide that  
 401 migrates to  $\sim 55$  km from the shoreline (Fig. 6). Rift shoulders are lowered down faster for higher  
 402 erodibility ( $< 1500$  m at 15 Ma) than for lower erodibility (2000 – 2500 m at 15 Ma).

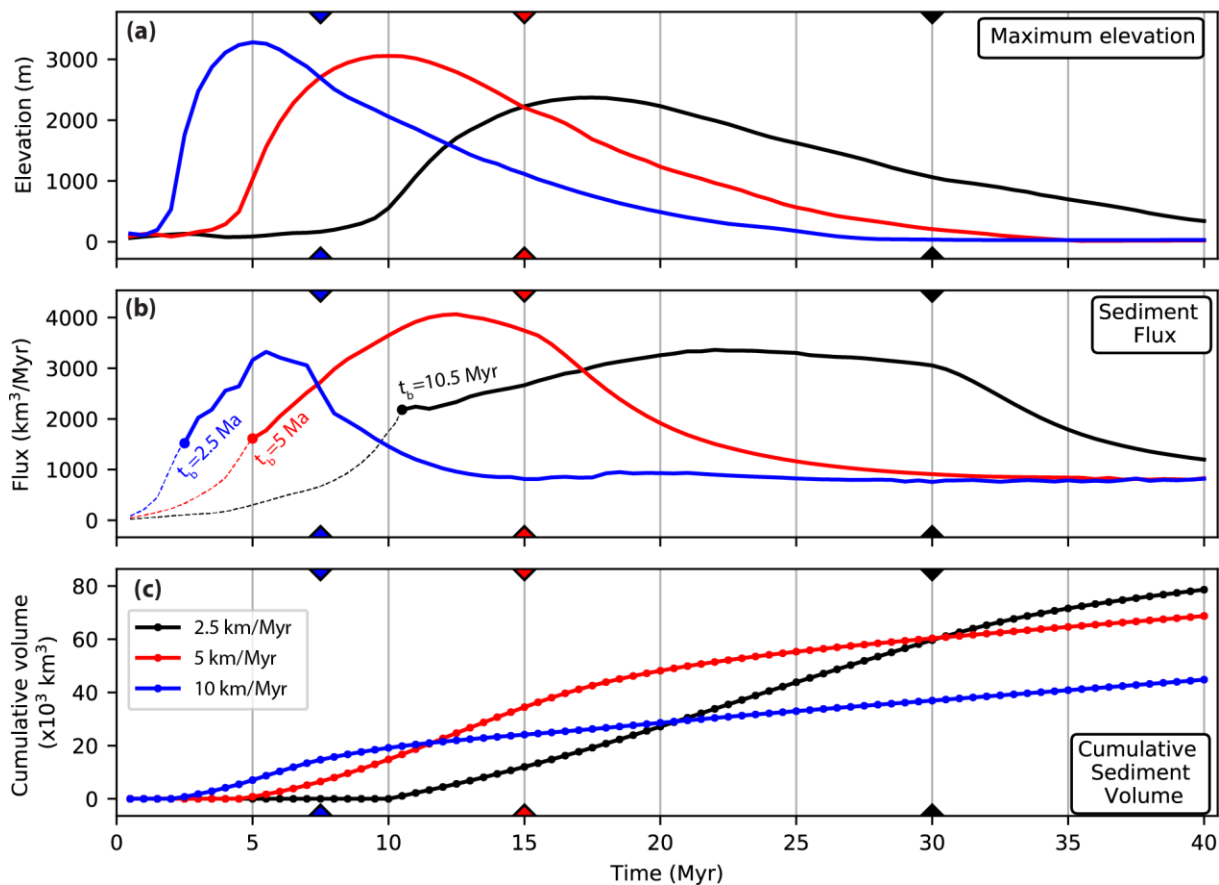
### 403 3.2 Sensitivity of elevation and sediment production to extension rate and erodibility

404 We next explore how varying extension rate and erodibility affect elevation and sediment production.

405 Models SM1, M1 and M2 (Table 1) explore the sensitivity to varying extension rates, equal to 2.5

406 km/Myr, 5 km/Myr, and 10 km/Myr, respectively, for identical erodibility  $k_f = 0.5 \times 10^{-5} \text{ m}^{0.2}/\text{yr}$  and

407 crustal strength R1 (Fig. 7). In contrast, models M4, SM3, M2 and M5 (Table 1) explore the effect of



408

409 **Figure 7: Influence of extension rate on the evolution of elevation (a), sediment flux (b) and sediment**  
 410 **volume (c).** Results are for models M1, M2, SM1 with high crustal strength, intermediate erosional efficiency ( $k_f$   
 411  $= 0.5 \times 10^{-5} \text{ m}^{0.2}/\text{yr}$ ), and variable extension rates/extension durations of 30 Myr (black), 15 Myr (red) and 7.5  
 412 Myr (blue). In all panels, the colored triangles indicate the end of extension of the respective model. Note that  
 413 sediment flux in the slowest model (2.5 km/Myr) does not reach a steady value within the 40 Myr simulation.  
 414 Sediment flux and volume are only recorded after the basin has reached sea level at time  $t_b$  (which depends on  
 415 the respective extension rate). Prior to  $t_b$  sediment is transported out of the model domain. The total volumes of  
 416 sediment lost this way are  $4952 \text{ km}^3$ ,  $2016 \text{ km}^3$ ,  $904 \text{ km}^3$  and  $322 \text{ km}^3$  for models with extension rates of 2.5  
 417 km/Myr, 5 km/Myr, 10 km/Myr and 15 km/Myr, respectively.

418

419 varying erodibility with  $k_f = 0.1, 0.25, 0.5, 1 \times 10^{-5} \text{ m}^{0.2}/\text{yr}$ , respectively for an identical extension rate  
 420 5 km/Myr and crustal strength R1 (Fig. 8).

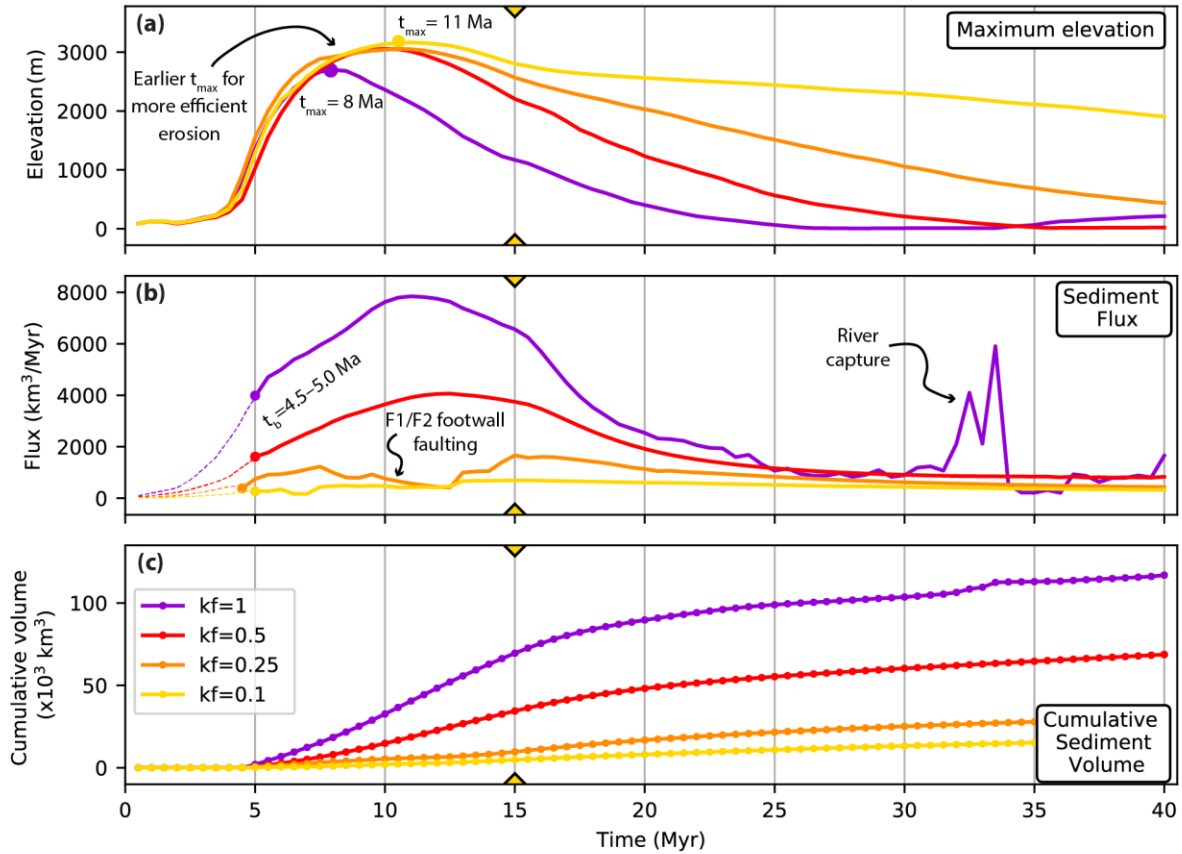
421 Maximum elevation follows a similar evolution for the models with variable extension rate with four  
 422 characteristic phases (Fig. 7a). During Phase 1, initial rifting with distributed deformation generates  
 423 almost no topography. Maximum topography increases rapidly during Phase 2 when deformation  
 424 localizes, and the main rift shoulders are uplifted (Fig. 7a). Maximum elevation is reached

425 systematically reached before the respective end of extension. The faster the extension rate, the earlier  
426 the peak, which is also slightly higher (Fig. 7a). During Phase 3, rift activity migrates to the centre of  
427 the basin, with maximum topography slowly decreasing towards the end of the syn-rift phase. After  
428 the end of extension, during Phase 4, elevation decays gradually and the rift shoulders are completely  
429 eroded away with a timescale depending primarily on fluvial erodibility (Fig. 7a, 8a).

430 Sediment flux similarly exhibits four characteristic phases in the models (Fig. 7b). Initial  
431 Phase 1 shows a slow increase of sediment flux with time. During Phase 2 sediment flux increases  
432 rapidly after the basin reaches sea level (time  $t_b$ ), and reaches a peak shortly after maximum  
433 topography is reached. Subsequently sediment flux decreases slowly during Phase 3 until the end of  
434 extension (Fig. 7b). The timing of peak sediment flux depends on the extension rate (Fig. 7b). During  
435 Phase 4 the sediment flux decreases exponentially to a steady state value 10 – 15 Myr after the end of  
436 extension (Fig. 7b). Cumulative sediment volume slowly increases with time and mirrors the evolution  
437 of sediment flux. At 40 Myr cumulative sediment volumes are notably higher for lower extension rates  
438 (Fig. 7c).

439 Models with varying erodibility (e.g., Fig. 8) show features similar to those with varying  
440 extension rate. All reach a maximum elevation of ~3000 m except for the high erodibility model that  
441 has maximum topography ~2800 m (Fig. 8a). The timing of maximum topography occurs earlier with  
442 increasing erodibility and occurs, in all cases, well before the end of extension. Subsequently, during  
443 the post-rift maximum elevation decreases progressively to a few hundreds of metres (Fig. 8a).

444 Maximum sediment flux is proportional to erosional efficiency (Figs. 8b,c). Models with  
445 varying erosional efficiency exhibit maximum sediment flux values of about 800, 1800, 4000, and  
446 8000 km<sup>3</sup>/Myr, respectively, for  $k_f$  ranging [0.1, 0.25, 0.5, 1.0] x 10<sup>-5</sup> m<sup>0.2</sup>/yr. Maximum sediment flux  
447 is systematically later than peak elevation. The case with high erodability ( $k_f = 1.0 \times 10^{-5}$  m<sup>0.2</sup>/yr)  
448 shows a sudden increase in sediment flux (> 6000 km<sup>3</sup>/Myr) at ~33 Ma, marking a river capture event  
449 (Fig. 8b). Cumulative sediment volume at 40 Ma increases with erodibility (from 20 to 120 x 10<sup>3</sup> km<sup>3</sup>;  
450 Fig. 8c).



451

452 **Figure 8: Influence of erosional efficiency on the evolution of elevation (a), sediment flux (b) and sediment**  
 453 **volume (c).** Results for models with high crustal strength, 15 Myr of extension and variable erosional  
 454 efficiencies of  $k_f = 0.1 \times 10^{-5} \text{ m}^{0.2}/\text{yr}$  (yellow),  $k_f = 0.25 \times 10^{-5} \text{ m}^{0.2}/\text{yr}$  (orange),  $k_f = 0.5 \times 10^{-5} \text{ m}^{0.2}/\text{yr}$  (red) and  $k_f$   
 455  $= 1 \times 10^{-5} \text{ m}^{0.2}/\text{yr}$  (purple). In all panels, the yellow triangles indicate the end of extension of the models. In  
 456 panel (a),  $t_{\text{max}}$  refers to the timing of maximum elevation, which occurs earlier for more efficient erosion.  
 457 Sediment flux and cumulative sediment volume are only recorded after the basin of the respective model has  
 458 reached sea level at time  $t_b$  (which varies between 4.5 – 5 Ma). Prior to  $t_b$  sediment is transported out of the  
 459 model domain. The total volumes of sediment lost this way are  $3358 \text{ km}^3$ ,  $2016 \text{ km}^3$ ,  $726 \text{ km}^3$  and  $393 \text{ km}^3$  (for  
 460 models with  $k_f$  values of 1, 0.5, 0.25 and  $0.1 \times 10^{-5} \text{ m}^{0.2}/\text{yr}$ , respectively). Note that sediment flux in model with  
 461 low erosional efficiency  $k_f = 0.25 \times 10^{-5} \text{ m}^{0.2}/\text{yr}$  exhibits several maxima and minima, due to fault activity in the  
 462 footwalls of F1 and F2, which lead to drainage reorganization (see Fig. 6)

463

#### 464 4 Discussion

465 In the following, we first discuss the first-order controls of rheology, extension rate, and surface  
 466 process efficiency on the evolution of modelled rifts. Next, we address how the different factors are  
 467 reflected in the sediment production and compare with natural rift examples. We then discuss

468 limitations of our modelling approach and compare our results to other modelling studies.

#### 469 **4.1 Influence of extension rate, rheology, and erodibility on rift evolution**

470 Our results show that the evolution of a rift is mostly controlled by the degree of strain localization.

471 High degree of strain localization results in a simpler rift geometry, with less active faults and more  
472 offset. Models M1 to M5 demonstrate how crustal rheology, surface process efficiency, and extension  
473 rate affect the degree of strain localization.

474 Comparison between model M1 with strong crust (Fig. 3) and M3 with intermediate crustal  
475 strength (Fig. 5) illustrates the effect of rheology on strain localization. Intermediate crustal strength  
476 limits the coupling between crust and mantle (Beucher & Huismans, 2020), and results in faults  
477 terminating at the top of the viscous middle crust (Fig. 5). The weaker coupling reduces strain  
478 localization and leads to a wide symmetric rift with multiple active faults with moderate offset. In  
479 contrast, strong crust promotes strain localization in a narrow rift with few large offset crustal-scale  
480 faults that connect to the strong upper mantle lithosphere (Figs. 3 and 4). Rift flank topography  
481 associated with footwall uplift is directly controlled by the amount of fault offset and by the strength  
482 of the crust. The strong crust cases promote large offset normal faults that generate high topography  
483 (>3000 m), while in contrast intermediate crustal strength cases promote reduced offset and lower rift  
484 flank topography (~1500 m).

485 The relative importance of tectonic uplift and erosion in the models can be understood  
486 considering the non-dimensional uplift-erosion number  $N_e$  (Whipple & Tucker, 1999) that can be  
487 formulated for  $n=1$  as  $N_e \propto U / (k_f \times h)$ , where  $U$  is tectonic uplift rate, and  $h$  is elevation.  $N_e$  only  
488 weakly scales with drainage area or river length, which are therefore omitted. This simple relationship  
489 shows that for large  $N_e$  uplift dominates over erosion, and vice versa for low  $N_e$ . We observe in our  
490 models that halving the extension rate (which reduces the uplift rates) has the same effect as doubling  
491  $k_f$ , both in terms of structure and sediment flux. This is easy to explain with  $N_e$ , because the resulting  
492 erosion number  $N_e$  will be the same when either halving the extension rate or doubling  $k_f$ . Similarly,  
493 models with strong rheology result in higher topography (3000 m) than those with intermediate  
494 rheology (1500 m). Accordingly, if we choose an intermediate rheology, we need to either half the

495 extension rate, or double  $k_f$  in order to obtain a similar  $N_e$ , that is, the same surface process efficiency.

496         The behavior of models M1, M2, M4, M5 is consistent with this simple scaling of the trade off  
497 and relative importance of extension rate that controls rock uplift rates along the main rift bounding  
498 faults and of fluvial erodibility that controls the rate of erosion of topography generated along these  
499 faults, counteracting rock uplift. Models M1 (fast extension, Fig. 3) and M2 (slow extension, Fig. 4),  
500 with an identical erodibility, show that slower extension promotes localization of deformation with  
501 only four active faults in model M2 with higher offset as compared to six faults in model M1. In  
502 contrast Models M2, M4, and M5 (Fig. 6) illustrate the effect of varying erodibility for an identical  
503 extension rate. Higher erodibility promotes strain localization resulting in fewer faults with more  
504 offset and more symmetric rifting. Erosional efficiency is increased for either a higher erodibility or  
505 for slower extension. A positive feedback between footwall erosion, hanging wall sedimentation, and  
506 fault offset has been demonstrated by earlier studies (e.g., Maniatis et al., 2009; Olive et al., 2014;  
507 Theunissen & Huisman, 2019). Our models show that a higher erosional efficiency increases this  
508 feedback owing to more erosion in the footwall and deposition in the hanging wall. Efficient erosion  
509 and deposition promote the evolution of large displacement boundary faults (Figs. 4 and 6). The  
510 increased offset on the boundary faults delays the basin-ward migration of deformation and limits the  
511 development of other faults. Intermediate crustal strength cases result in lower rift shoulders resulting  
512 in lower surface process efficiency given the same  $k_f$  value, which limits the feedback between  
513 tectonic uplift and erosion.

514         In summary, rheology, extension rate, and erodibility impact the structural evolution of rifts.  
515 For a given erodibility, a stronger crust and slower extension increase strain localization: less faults are  
516 active, more fault offset is generated, the rift is more symmetric, and the feedback between erosion and  
517 deposition is stronger. This, in turn, also has important implications for the evolution of the sediment  
518 production of rift systems, further discussed below.

## 519 **4.2 Sediment production of the rift**

### 520 **4.2.1 Total volume of sediment**

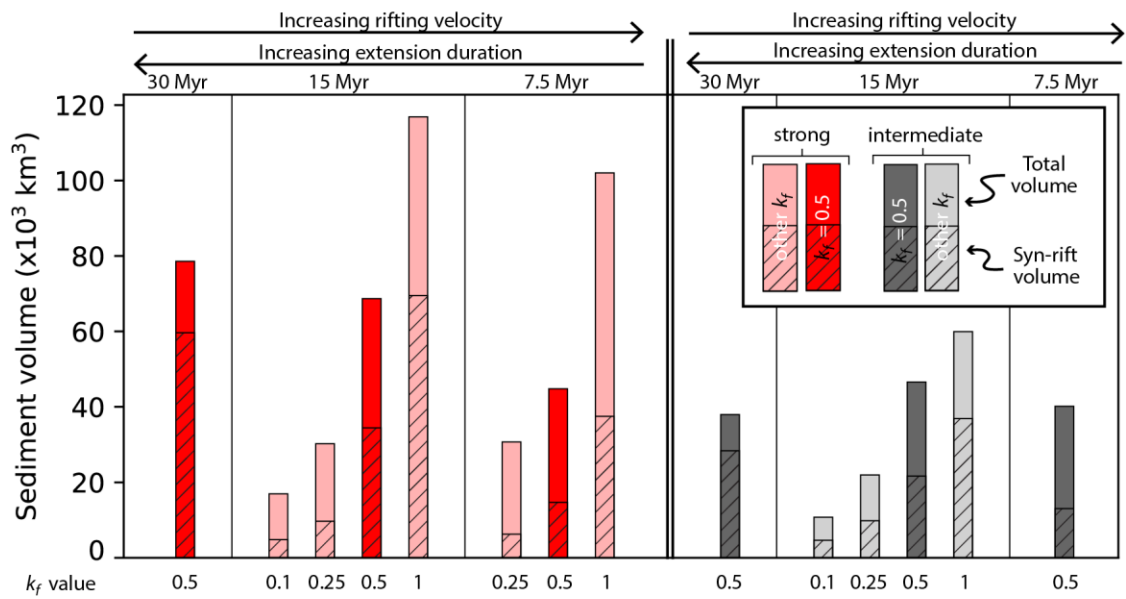
521         The amount of sediment produced during rifting scales with (1) topography, and (2) surface

522 process efficiency. Syn-rift tectonic rock uplift generates elevated rift shoulders and fluvial erosion  
523 provides the main source of sediments. During the post-rift, rivers can capture the hinterland drainage  
524 network, yielding additional sediment. These two sources of sediment depend on the evolution of the  
525 rift and the total sediment volume is controlled by rift structural style and rheology, by extension rate,  
526 and by erodibility. Fig. 9 summarizes the volumes of sediment produced after 40 Myr of simulation  
527 for all models (M1 to M5 and SM1 to SM9, Table 1).

528 As expected, for a strong crust and a given extension rate (for instance for models with 15  
529 Myr of extension), a higher erodibility increases the total sediment volume (Fig. 9). However, for a  
530 given erodibility, slower extension models with lower topography and rock uplift rates (i.e., 30 and 15  
531 Myr of extension) yield substantially more sediment ( $70 - 80 \times 10^3 \text{ km}^3$ ), than faster extension models  
532 with higher topography and rock uplift rates (i.e.,  $45 \times 10^3 \text{ km}^3$  for 7.5 of extension; Fig. 9). This is  
533 intuitive, as the volume of generated sediment scales with the magnitude of topography and  
534 cumulative rock uplift; the latter is higher for lower extension rates (Figs 3 and 4). Slower extension  
535 localizes deformation on fewer structures sustaining more fault offset over a longer duration and can  
536 be explained by the more efficient feedback between continued fault localization and surface processes  
537 at lower extension rates (Figs. 7 and 9).

538 For intermediate crustal strength, higher erodibility similarly increases the total sediment  
539 volume (Fig. 9). However, comparison between models with intermediate and high crustal strength  
540 shows that cases with stronger crust generate 10 – 100 % more sediment (e.g., models M1 vs. M3 or  
541 M5 vs. SM7, Fig. 9). Lower fault offset and associated footwall uplift for the intermediate crustal  
542 strength cases limits the feedback between erosion and deformation and the lower maximum elevation  
543 of the rift shoulders results in lower sediment volumes.

544 The amount of syn-rift sediment relative to the total sediment volume increases systematically  
545 with increasing erodibility, irrespective of the rheology and extension rate (Fig. 9). This effect is  
546 stronger for lower rates of extension, as the feedback between erosion/deformation is stronger. For  
547 example, models with intermediate extension duration (15 Myr) and erodibility (i.e., models M2, M5  
548 and SM7 with  $k_f \geq 0.5 \times 10^{-5} \text{ m}^{0.2}/\text{yr}$ ), produce over 50 % of the total sediment volume during the syn-  
549 rift. This results in a rift, where the majority of sediment is deposited during active deformation and



550

551 **Figure 9: Sediment volumes generated during rifting.** Comparison of the sediment volumes (deposited since  
 552 the basin has reached sea level) for the 14 models (Table 1). Models are grouped according to their rheology (red  
 553 = strong, R1; grey = intermediate, R2) and subsequently ordered with respect to extension duration/rate. Models  
 554 with dark-colored bars share the same  $k_f$  value (i.e.,  $k_f = 0.5$ ), in order to easily compare the sediment volumes  
 555 for models with the same intermediate erosional efficiency. Models with other  $k_f$  values (i.e., 0.1, 0.25 and 1) are  
 556 pale colored. For each model, the height of the bar indicates the total sediment volume, whereas the height of the  
 557 hatched bar indicates the synrift volume.

558

559 subjected to faulting.

560 For the models with very high erodibility (i.e.,  $k_f = 1 \times 10^{-5} \text{ m}^{0.2}/\text{yr}$ ), river capture events  
 561 during the post-rift phase may result in a transient increase of the volume of sediment delivered to the  
 562 basin. However, the volume of sediment generated by river capture is small compared to that  
 563 generated during the syn-rift phase (i.e., Fig. 8c).

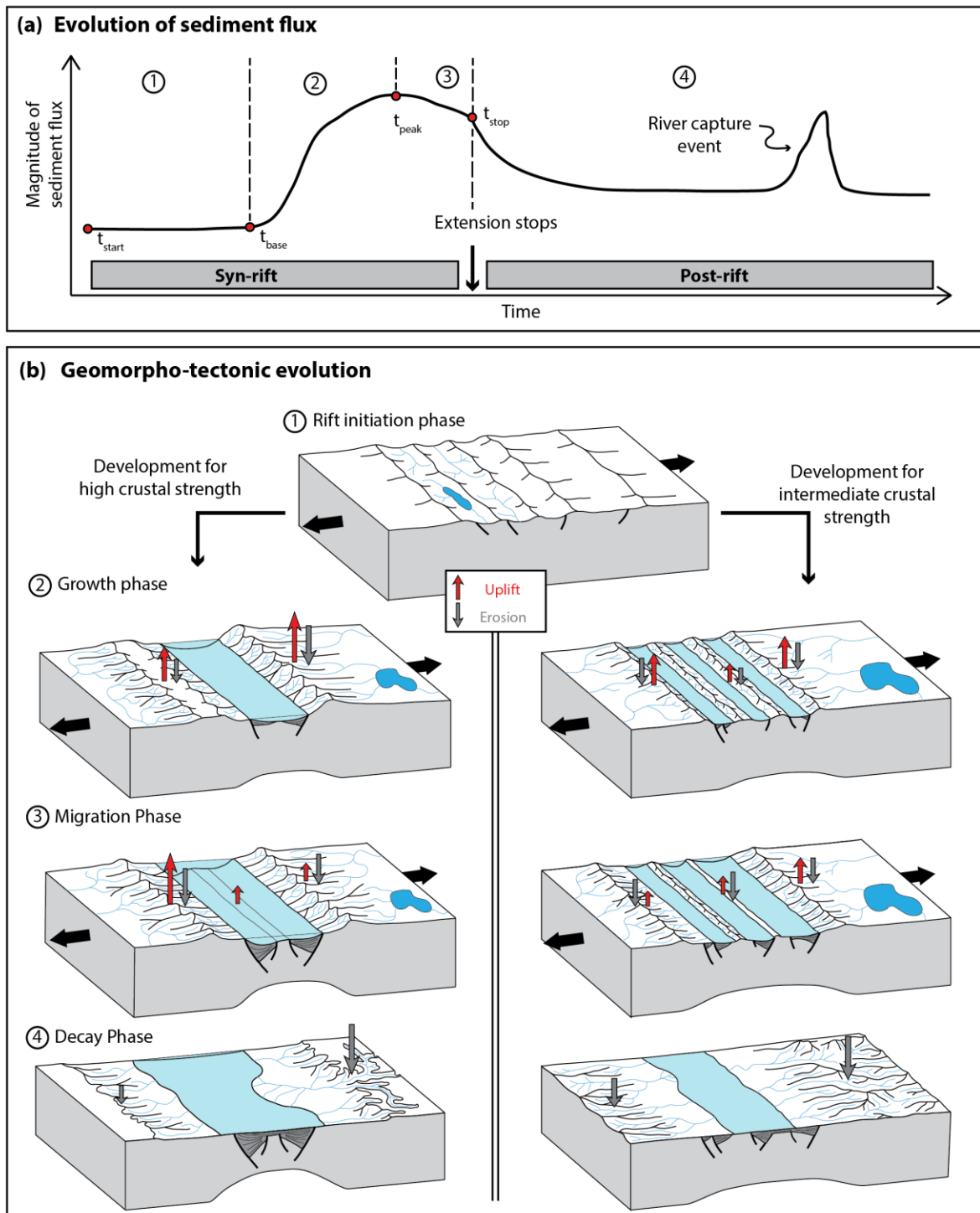
564 In summary, total sediment volume produced during rift evolution primarily reflects the  
 565 combined effects of strain localization and erodibility. Slow extension, strong crust, and efficient  
 566 surface processes yield higher total volumes of sediment. For a given erodibility, a reduction of 50%  
 567 in the extension rate results in a 15 to 40 % higher sediment volume (Fig. 9). Sediment volume is  
 568 directly proportional to erodibility (Fig. 9). Efficient erosion increases the proportion of syn-rift to  
 569 post-rift sediments (Fig. 9). These observations point toward a complex interaction of tectonic and  
 570 surface processes controlling sediment production. A rift system may generate a large amount of

571 sediment based on its tectonic boundary conditions (i.e., the degree of strain localization could be  
572 high, because the crust is strong, and extension is slow). Low erosional efficiency may in turn affect  
573 the degree of strain localization limiting the feedback between deformation and erosion and reducing  
574 sediment production.

#### 575 **4.2.2 Temporal evolution of rift structure, sediment flux, and comparison to natural cases**

576 The evolution of rift structure and associated sediment flux (Fig. 10a) follows four distinct temporal  
577 geomorpho-tectonic phases (Fig. 10b). Phase 1 early-stage rift initiation is marked by distributed  
578 deformation, limited offset on several faults that produces little elevation, and low erosion rates,  
579 generating little sediment. Growth Phase 2 exhibits localization of deformation on the main rift  
580 bounding faults with rapid rift flank uplift, basin subsidence, river incision into the uplifting rift flanks,  
581 and steep relief resulting in high erosion rates and a strong increase in sediment flux. Phase 3 basin-  
582 ward migration of fault activity, associated with a decrease in uplift and erosion rates, is characterized  
583 by sediment flux slowly decreasing from its peak. After the end of extension, decay Phase 4 shows  
584 exponential decrease in sediment flux reflecting post rift fluvial erosion of rift flank topography and  
585 landward migration of river divides. Drainage capture of the hinterland during Phase 4 may lead to a  
586 transient increase in sediment flux. These four phases can be recognized in both strong and  
587 intermediate crustal strength models. In the case of intermediate crustal strength, the general trend of  
588 the flux is similar, but the magnitude of the different peaks is lower compared to the high crustal  
589 strength case (Fig. S4 and S5).

590 We suggest that the phases of rifting shown by our models reproduce many characteristics of  
591 natural rift systems. Phases 1 to 3 can be recognized in the northern North Sea (Fazlikhani et al., 2021;  
592 Fossen et al., 2021), where deformation was initially distributed over several 100s of kilometers of  
593 width (e.g., Phase 1), before localizing on the boundary faults that accommodate most of the strain  
594 forming a 150 km wide rift (Phase 2), and subsequent basin-ward migration of deformation at the end  
595 of the syn-rift (e.g., Phase 3) (Fazlikhani et al., 2021). Similarly, the Gulf of Suez (Gawthorpe et al.,  
596 2003) exhibits both initial distributed deformation (Phase 1), followed by localization of deformation  
597 on the boundary faults (Phase 2), and a subsequent basin-ward shift in deformation (Phase 3). The  
598 Gulf of Corinth exhibits an initial phase of wide distributed extension (Phase 1) before shifting



599

600 **Figure 10: Evolution of the sediment flux related to rifting phases.** (a) General evolution of the sediment flux  
 601 subdivided into four phases, and (b) cartoons of the four geomorpho-tectonic phases of the rift. After an initial  
 602 phase of distributed deformation (Phase 1), the rifts have a different tectonic and topographic evolution (Phase 2  
 603 to 4), depending on the crustal strength: The left column displays the evolution in case of a high crustal strength,  
 604 the right column in case of intermediate crustal strength. Red arrows indicate the magnitude of rock uplift, and  
 605 grey arrows the magnitude of erosion, such that if uplift exceeds erosion the surface is uplifting, and when  
 606 erosion exceeds uplift the surface is lowered.

607 deformation into the present day Gulf (Phase 2/3) (Ford et al., 2017; Gawthorpe et al., 2018).

608 Full coverage of the evolution of sediment flux for the active stages of rifting is scarce for  
609 natural examples. However, the Gulf of Suez and Lake Albert rift provide sufficient data coverage and  
610 corroborate our proposed pattern. In the Gulf of Suez, the syn-rift peak in sediment flux coincides with  
611 the rift climax (Phase 2-3), with a strong decrease to low steady sediment flux in the post-rift (Phase  
612 4), followed by a second, climate-induced peak in sediment flux (Rohais et al., 2016; Rohais & Rouby,  
613 2020). The Lake Albert rift (East African Rift system) exhibits low sedimentation rates during the first  
614 11 Myr of slow extension (Phase 1) (Simon, 2015), followed by a strong increase and maximum  
615 sedimentation rates during the next 4 Myr, reflecting localization and increased fault offset on the  
616 main rift boundary fault (Phase 2). Lastly, a major river capture event, characteristic for Phase 4,  
617 explains the increase in sediment flux in the Zambezi Delta of the East Africa rifted margin (Walford  
618 et al., 2005).

619 The BQART method (Syvitski & Milliman, 2007) that empirically relates present-day values  
620 of sediment flux of modern river systems to relief, catchment area, and climatic factors, is used to  
621 invert the evolution of sediment flux to infer the past topographic evolution of rifts (e.g., Rohais &  
622 Rouby, 2020; Sømme et al., 2019). Our model results allow independent validation of the BQART  
623 method on geologic timescales. We use maximum topography as a measure of relief and compare this  
624 to the sediment flux of our models. Peak elevation systematically predates peak sediment flux by 1 – 3  
625 Myr in models with sufficiently high erosion for a river network to develop (Figs. 7 and 8). The  
626 magnitude in peak sediment flux correlates strongly with erodibility consistent with the climatic  
627 factors in the BQART method. These observations show that long time scale temporal changes in  
628 sediment flux reflect coeval changes in topography, consistent with one of the basic assumptions of  
629 the BQART method. However, the magnitude of the peak in sediment flux does not necessarily scale  
630 with the magnitude of topography, indicating a complex relationship between the sediment flux and  
631 relief/topography. This is in accordance with observations from Brewer et al. (2020) suggesting that  
632 relief and paleo-topography are a significant source of uncertainty for estimation of sediment flux with  
633 the BQART method. In our models, the magnitude of topography is mostly sensitive to crustal  
634 strength and to a lesser degree to extension rate. Both peak sediment flux and cumulative sediment

635 volume are critically dependent on the feedback between erosion, deposition, and fault offset. A  
636 system with a strong feedback, i.e. slow extension combined with high erodibility, yields more  
637 sediment, compared to a system with fast extension, higher rock uplift rates and topography, and a  
638 weaker feedback. In natural systems independent constraints on tectonic and climatic boundary  
639 conditions and their effect on topography and sediment flux may help to refine the BQART method  
640 for reconstructing the topographic evolution of rifts from the sedimentary record. Our results also  
641 demonstrate a time lag between peak rock uplift rate, topography, and sediment flux, which is mostly a  
642 function of the extension rate (Fig. 7, S3a). If the extension rate is low, peak uplift rate precedes the  
643 major pulse in sediment that is delivered to a basin by several million years (e.g., 5 Myr for model  
644 M2). This may help to refine the understanding and interpretation of sedimentary records, when it  
645 comes to attributing changes in sediment flux to tectonic events.

646 In summary, the temporal evolution of the sediment flux follows a distinctive pattern. It  
647 reflects the successive phases of the tectonic and geomorphic evolution of the rift system, which can  
648 also be observed in natural systems. The magnitude of the peak in sediment flux depends on the  
649 erosional efficiency, but also on the magnitude of topography as controlled by crustal rheology. The  
650 duration of the phases and the timing of the sediment flux peak(s) depend on the extension rate and the  
651 erosional efficiency.

#### 652 **4.3 Comparison with previous model work and limitations of our modelling approach**

653 Earlier studies investigated continental extension using numerical models, emphasizing the evolution  
654 of the late stages of rifting or passive margin formation. Several of these studies focused on the role of  
655 crustal rheology and surface processes (e.g., Andrés-Martínez et al., 2019; Beucher & Huismans,  
656 2020; Buitter et al., 2008; Theunissen & Huismans, 2019), whereas others focused on the interplay of  
657 crustal rheology and extension rate (e.g., Naliboff et al., 2017; Svartman Dias et al., 2015; Tetreault &  
658 Buitter, 2018). Our study is the first to test the sensitivity of continental rifting and the associated  
659 surface process response to the combined effects of crustal rheology, extension rate, and erodibility.

660 Our results corroborate the role of crustal rheology controlling the coupling between crust and  
661 mantle, with stronger coupling resulting in more localized and focused deformation (e.g., Theunissen  
662 & Huismans, 2019) leading to higher elevation of the rift shoulders (e.g., Beucher & Huismans, 2020;

663 Tetreault & Buitter, 2018). Extension rate and erodibility have a subordinate control on crust-mantle  
664 coupling. For a strong coupling, we observe asymmetric rifts (in terms of fault offset and elevation)  
665 during the initial stages of rifting, irrespective of the extension rate. However, in case of slower  
666 extension enhanced offset along the second rift bounding fault leads to symmetric rift structure  
667 towards the end of extension.

668 The feedback effect between erosion, sedimentation, and deformation during rifting has been  
669 described in earlier studies (Andrés-Martínez et al., 2019; Buitter et al., 2008; Maniatis et al., 2009;  
670 Olive et al., 2014; Theunissen & Huismans, 2019). Also in our case, stronger surface processes lead to  
671 more strain localization (Andrés-Martínez et al., 2019), more fault offset and prolonged fault activity  
672 (Beucher & Huismans, 2020; Olive et al., 2014; Theunissen & Huismans, 2019) and more symmetric  
673 basins with fewer active faults (Buitter et al., 2008). In addition, we show that the feedback of surface  
674 processes on tectonics is stronger for slower (but longer duration) extension, resulting in larger fault  
675 offset, generating more sediment.

676 Our models have the following inherent limitations: We do not include temporal or spatial  
677 variations of erodibility in our models and 3D effects of deformation are excluded owing to the 2D  
678 nature of the thermo-mechanical model. We only consider sedimentation offshore below sea level, and  
679 no material is deposited in the continental domain. Thus, any onshore sediment that could be  
680 remobilized later on, is not considered in our analysis of the sediment flux or the total sediment  
681 volume. No material is deposited during the early stages of rifting before the basin has reached sea  
682 level and sediment produced during this time leaves the model domain. However, not including the  
683 sediment generated during early rifting does not significantly change total sediment volume estimates.

## 684 **5 Conclusions**

685 We use a thermo-mechanical model coupled with a landscape evolution model to investigate the  
686 evolution of continental rifts. Our models aim at resolving the evolution of tectonic activity, the  
687 associated topography and sediment production during rifting, and how they are affected by the  
688 tectonic and surface processes boundary conditions. We show that the degree of strain localization is  
689 critical for the evolution of a rift, and that it is controlled by crustal rheology, extension rate, and  
690 erodibility. Our results corroborate that an increase in erodibility promotes a strong coupling between

691 tectonic and surface processes, through the feedback between footwall erosion, hanging wall  
692 deposition, and increased fault offset. We demonstrate that for an intermediate crustal strength, weak  
693 coupling between crust and mantle limits fault offset, which reduces the efficiency of the feedback.  
694 Feedback between tectonics and surface processes is strongest for slower and extended extension  
695 owing to lower uplift rates and prolonged fault activity. Slowly extending rift systems with strong  
696 crust and efficient erosion exhibit a strong coupling between tectonics and surface processes, resulting  
697 in a structurally simple rift, with large fault offset and high sediment production. We reach the  
698 following specific conclusions:

- 699 1. Structure, topography, and sediment volume of the rifts are primarily controlled by the degree of  
700 strain localization.
- 701 2. Rift systems with strong crust and a high degree of strain localization generate the highest  
702 sediment volumes. For a given erodibility, slower extending rifts produce more sediment than  
703 faster extending rifts, such that a reduction in extension rate by 50% increases the amount of  
704 sediment by 15 – 40 %.
- 705 3. Feedback between erosion and deformation increases fault offset, enhancing rock uplift, and  
706 yielding more sediment. The effect is strongest for systems with efficient erosion (slow extension  
707 and high erodibility) and limited if the coupling between crust and mantle is low.
- 708 4. We identify four characteristic phases for the evolution of sediment flux. Phase 1 early-stage rift  
709 initiation is associated with low topography, erosion rates, generating little sediment. Phase 2 rift  
710 growth is associated with uplift along the main rift bounding faults resulting in high erosion rates  
711 and a strong increase in sediment flux. Phase 3 basin-ward migration of fault activity is associated  
712 with slowly decreasing sediment flux. Post rift Phase 4 displays exponential decrease in sediment  
713 flux. Drainage capture of the hinterland during Phase 4 may lead to a transient increase in  
714 sediment flux. The phases of rifting reproduce many characteristics of natural rift systems and can  
715 be, for example, recognized in the northern North Sea, the Gulf of Suez, and the Gulf of Corinth.
- 716 5. Our modelling results indicate that for natural examples, the approach of inverting the sedimentary  
717 record for the topographic evolution of rifts is promising. However, the peaks in rock  
718 uplift/maximum elevation predate the peak in sediment flux by 2 – 5 Myr (depending on the

719 extension rate).

720 In summary, the evolution of a rift in terms of structures, topography and sediment flux reflects  
721 the complex interactions that can occur between tectonic and surface processes. We suggest that future  
722 work could include a more detailed analysis of geomorphic metrics (e.g., catchment area) or of the  
723 stratigraphic architecture. A comparison of these metrics from the model output with natural cases  
724 could also lead to a better understanding of the complicated processes behind continental rifting.

#### 725 **Acknowledgements:**

726 The work presented in this study was funded by Total Energies through the COLORS project. We  
727 acknowledge computational resources by Uninett Sigma2 for project NN4704K. We thank Thomas  
728 Theunissen for fruitful discussions and his help for setting up the strain inheritance of the models. We  
729 also acknowledge discussions with Brendan Simon about the geology and sedimentary history of Lake  
730 Albert.

#### 731 **Open research**

732 As earth surface process model, we use the freely-available, open source code FastScape  
733 (<https://fastscape.org/>), as outlined in the methods section. As thermo-mechanical model, we use the  
734 code Fantom (Thielot, 2011), using the equations and procedure as outlined in the methods section. In  
735 the supplementary material, we provide animations of all 14 models containing the essential data for  
736 our analyses.

737

#### 738 **References**

- 739 Adams, B. A., Hodges, K. V., Whipple, K. X., Ehlers, T. A., van Soest, M. C., & Wartho, J. (2015).  
740 Constraints on the tectonic and landscape evolution of the Bhutan Himalaya from  
741 thermochronometry: Late Cenozoic Evolution of Bhutan. *Tectonics*, 34(6), 1329–1347.  
742 <https://doi.org/10.1002/2015TC003853>
- 743 Allen, P. A. (2008). Time scales of tectonic landscapes and their sediment routing systems. *Geological*  
744 *Society, London, Special Publications*, 296(1), 7–28. <https://doi.org/10.1144/SP296.2>
- 745 Allen, P. A., & Heller, P. L. (2011). Dispersal and Preservation of Tectonically Generated Alluvial  
746 Gravels in Sedimentary Basins. In *Tectonics of Sedimentary Basins* (pp. 111–130). John Wiley  
747 & Sons, Ltd. <https://doi.org/10.1002/9781444347166.ch6>

- 748 Andrés-Martínez, M., Pérez-Gussinyé, M., Armitage, J., & Morgan, J. P. (2019). Thermomechanical  
749 Implications of Sediment Transport for the Architecture and Evolution of Continental Rifts  
750 and Margins. *Tectonics*, 38(2), 641–665. <https://doi.org/10.1029/2018TC005346>
- 751 Armitage, J. J., Duller, R. A., Whittaker, A. C., & Allen, P. A. (2011). Transformation of tectonic and  
752 climatic signals from source to sedimentary archive. *Nature Geoscience*, 4(4), 231–235.  
753 <https://doi.org/10.1038/ngeo1087>
- 754 Beaumont, C., Fullsack, P., & Hamilton, J. (1992). Erosional control of active compressional orogens.  
755 In K. R. McClay (Ed.), *Thrust Tectonics* (pp. 1–18). Dordrecht: Springer Netherlands.  
756 [https://doi.org/10.1007/978-94-011-3066-0\\_1](https://doi.org/10.1007/978-94-011-3066-0_1)
- 757 Beucher, R., & Huismans, R. S. (2020). Morphotectonic Evolution of Passive Margins Undergoing  
758 Active Surface Processes: Large-Scale Experiments Using Numerical Models. *Geochemistry,*  
759 *Geophysics, Geosystems*, 21(5). <https://doi.org/10.1029/2019GC008884>
- 760 Braun, J., & Willett, S. D. (2013). A very efficient O(n), implicit and parallel method to solve the  
761 stream power equation governing fluvial incision and landscape evolution. *Geomorphology*,  
762 180–181, 170–179. <https://doi.org/10.1016/j.geomorph.2012.10.008>
- 763 Brewer, C. J., Hampson, G. J., Whittaker, A. C., Roberts, G. G., & Watkins, S. E. (2020). Comparison  
764 of methods to estimate sediment flux in ancient sediment routing systems. *Earth-Science*  
765 *Reviews*, 207, 103217. <https://doi.org/10.1016/j.earscirev.2020.103217>
- 766 Buiter, S. J. H., Huismans, R. S., & Beaumont, C. (2008). Dissipation analysis as a guide to mode  
767 selection during crustal extension and implications for the styles of sedimentary basins.  
768 *Journal of Geophysical Research: Solid Earth*, 113(B6).  
769 <https://doi.org/10.1029/2007JB005272>
- 770 Castelltort, S., & Van Den Driessche, J. (2003). How plausible are high-frequency sediment supply-  
771 driven cycles in the stratigraphic record? *Sedimentary Geology*, 157(1–2), 3–13.  
772 [https://doi.org/10.1016/S0037-0738\(03\)00066-6](https://doi.org/10.1016/S0037-0738(03)00066-6)
- 773 Champagnac, J.-D., Molnar, P., Sue, C., & Herman, F. (2012). Tectonics, climate, and mountain  
774 topography. *Journal of Geophysical Research: Solid Earth*, 117(B2), n/a-n/a.  
775 <https://doi.org/10.1029/2011JB008348>
- 776 Corti, G., Molin, P., Sembroni, A., Bastow, I. D., & Keir, D. (2018). Control of Pre-rift Lithospheric  
777 Structure on the Architecture and Evolution of Continental Rifts: Insights From the Main  
778 Ethiopian Rift, East Africa. *Tectonics*, 37(2), 477–496. <https://doi.org/10.1002/2017TC004799>
- 779 Culling, W. E. H. (1963). Soil Creep and the Development of Hillside Slopes. *The Journal of Geology*,  
780 71(2), 127–161. <https://doi.org/10.1086/626891>
- 781 Densmore, A. L., Allen, P. A., & Simpson, G. (2007). Development and response of a coupled  
782 catchment fan system under changing tectonic and climatic forcing. *Journal of Geophysical*  
783 *Research*, 112(F1). <https://doi.org/10.1029/2006JF000474>
- 784 Enkelmann, E., Zeitler, P. K., Pavlis, T. L., Garver, J. I., & Ridgway, K. D. (2009). Intense localized

785 rock uplift and erosion in the St Elias orogen of Alaska. *Nature Geoscience*, 2(5), 360–363.  
786 <https://doi.org/10.1038/ngeo502>

787 Erdős, Z., Huismans, R. S., & van der Beek, P. (2015). First-order control of syntectonic  
788 sedimentation on crustal-scale structure of mountain belts. *Journal of Geophysical Research:*  
789 *Solid Earth*, 120(7), 5362–5377. <https://doi.org/10.1002/2014JB011785>

790 Fazlikhani, H., Aagotnes, S. S., Refvem, M. A., Hamilton-Wright, J., Bell, R. E., Fossen, H., et al.  
791 (2021). Strain migration during multiphase extension, Stord Basin, northern North Sea rift.  
792 *Basin Research*, 33(2), 1474–1496. <https://doi.org/10.1111/bre.12522>

793 Ford, M., Hemelsdaël, R., Mancini, M., & Palyvos, N. (2017). Rift migration and lateral propagation:  
794 evolution of normal faults and sediment-routing systems of the western Corinth rift (Greece).  
795 *Geological Society, London, Special Publications*, 439(1), 131–168.  
796 <https://doi.org/10.1144/SP439.15>

797 Forzoni, A., Storms, J. E. A., Whittaker, A. C., & de Jager, G. (2014). Delayed delivery from the  
798 sediment factory: modeling the impact of catchment response time to tectonics on sediment  
799 flux and fluvio-deltaic stratigraphy. *Earth Surface Processes and Landforms*, 39(5), 689–704.  
800 <https://doi.org/10.1002/esp.3538>

801 Fossen, H., Ksienzyk, A. K., Rotevatn, A., Bauck, M. S., & Wemmer, K. (2021). From widespread  
802 faulting to localised rifting: Evidence from K-Ar fault gouge dates from the Norwegian North  
803 Sea rift shoulder. *Basin Research*, 33(3), 1934–1953. <https://doi.org/10.1111/bre.12541>

804 Gawthorpe, R. L., Jackson, C. A.-L., Young, M. J., Sharp, I. R., Moustafa, A. R., & Leppard, C. W.  
805 (2003). Normal fault growth, displacement localisation and the evolution of normal fault  
806 populations: the Hammam Faraun fault block, Suez rift, Egypt. *Journal of Structural Geology*,  
807 25(6), 883–895. [https://doi.org/10.1016/S0191-8141\(02\)00088-3](https://doi.org/10.1016/S0191-8141(02)00088-3)

808 Gawthorpe, R. L., Leeder, M. R., Kranis, H., Skourtsos, E., Andrews, J. E., Henstra, G. A., et al.  
809 (2018). Tectono-sedimentary evolution of the Plio-Pleistocene Corinth rift, Greece. *Basin*  
810 *Research*, 30(3), 448–479. <https://doi.org/10.1111/bre.12260>

811 Geurts, A. H., Whittaker, A. C., Gawthorpe, R. L., & Cowie, P. A. (2020). Transient landscape and  
812 stratigraphic responses to drainage integration in the actively extending central Italian  
813 Apennines. *Geomorphology*, 353, 107013. <https://doi.org/10.1016/j.geomorph.2019.107013>

814 Gleason, G. C., & Tullis, J. (1995). A flow law for dislocation creep of quartz aggregates determined  
815 with the molten salt cell. *Tectonophysics*, 247(1), 1–23. [https://doi.org/10.1016/0040-](https://doi.org/10.1016/0040-1951(95)00011-B)  
816 [1951\(95\)00011-B](https://doi.org/10.1016/0040-1951(95)00011-B)

817 Grujic, D., Coutand, I., Bookhagen, B., Bonnet, S., Blythe, A., & Duncan, C. (2006). Climatic forcing  
818 of erosion, landscape, and tectonics in the Bhutan Himalayas. *Geology*, 34(10), 801–804.  
819 <https://doi.org/10.1130/G22648.1>

820 Guillocheau, F., Rouby, D., Robin, C., Helm, C., Rolland, N., Le Carlier de Veslud, C., & Braun, J.  
821 (2012). Quantification and causes of the terrigenous sediment budget at the scale of a

822 continental margin: a new method applied to the Namibia-South Africa margin: Quantification  
823 and causes of the terrigenous sediment budget at the scale of a continental margin. *Basin*  
824 *Research*, 24(1), 3–30. <https://doi.org/10.1111/j.1365-2117.2011.00511.x>

825 Hemelsdaël, R., Ford, M., Malartre, F., & Gawthorpe, R. (2017). Interaction of an antecedent fluvial  
826 system with early normal fault growth: Implications for syn-rift stratigraphy, western Corinth  
827 rift (Greece). *Sedimentology*, 64(7), 1957–1997. <https://doi.org/10.1111/sed.12381>

828 Huismans, R. S., & Beaumont, C. (2002). Asymmetric lithospheric extension: The role of frictional  
829 plastic strain softening inferred from numerical experiments. *Geology*, 30(3), 211–214.  
830 [https://doi.org/10.1130/0091-7613\(2002\)030<0211:ALETRO>2.0.CO;2](https://doi.org/10.1130/0091-7613(2002)030<0211:ALETRO>2.0.CO;2)

831 Huismans, R. S., & Beaumont, C. (2003). Symmetric and asymmetric lithospheric extension: Relative  
832 effects of frictional-plastic and viscous strain softening. *Journal of Geophysical Research:*  
833 *Solid Earth*, 108(B10). <https://doi.org/10.1029/2002JB002026>

834 Huismans, R. S., & Beaumont, C. (2011). Depth-dependent extension, two-stage breakup and cratonic  
835 underplating at rifted margins. *Nature*, 473(7345), 74–78. <https://doi.org/10.1038/nature09988>

836 Karato, S., & Wu, P. (1993). Rheology of the Upper Mantle: A Synthesis. *Science*, 260(5109), 771–  
837 778. <https://doi.org/10.1126/science.260.5109.771>

838 Li, Q., Gasparini, N. M., & Straub, K. M. (2018). Some signals are not the same as they appear: How  
839 do erosional landscapes transform tectonic history into sediment flux records? *Geology*, 46(5),  
840 407–410. <https://doi.org/10.1130/G40026.1>

841 Mackwell, S. J., Zimmerman, M. E., & Kohlstedt, D. L. (1998). High-temperature deformation of dry  
842 diabase with application to tectonics on Venus. *Journal of Geophysical Research: Solid Earth*,  
843 103(B1), 975–984. <https://doi.org/10.1029/97JB02671>

844 Maniatis, G., Kurfeß, D., Hampel, A., & Heidbach, O. (2009). Slip acceleration on normal faults due  
845 to erosion and sedimentation — Results from a new three-dimensional numerical model  
846 coupling tectonics and landscape evolution. *Earth and Planetary Science Letters*, 284(3–4),  
847 570–582. <https://doi.org/10.1016/j.epsl.2009.05.024>

848 McNeill, L. C., Shillington, D. J., Carter, G. D. O., Everest, J. D., Gawthorpe, R. L., Miller, C., et al.  
849 (2019). High-resolution record reveals climate-driven environmental and sedimentary changes  
850 in an active rift. *Scientific Reports*, 9(1), 3116. <https://doi.org/10.1038/s41598-019-40022-w>

851 Michel, L., Ehlers, T. A., Glotzbach, C., Adams, B. A., & Stübner, K. (2018). Tectonic and glacial  
852 contributions to focused exhumation in the Olympic Mountains, Washington, USA. *Geology*,  
853 46(6), 491–494. <https://doi.org/10.1130/G39881.1>

854 Molnar, P., & England, P. (1990). Late Cenozoic uplift of mountain ranges and global climate change:  
855 chicken or egg? *Nature*, 346(6279), 29–34. <https://doi.org/10.1038/346029a0>

856 Naliboff, J. B., Buiter, S. J. H., Péron-Pinvidic, G., Osmundsen, P. T., & Tetreault, J. (2017). Complex  
857 fault interaction controls continental rifting. *Nature Communications*, 8(1), 1179.  
858 <https://doi.org/10.1038/s41467-017-00904-x>

859 Olive, J.-A., Behn, M. D., & Malatesta, L. C. (2014). Modes of extensional faulting controlled by  
860 surface processes: Normal faulting and surface processes. *Geophysical Research Letters*,  
861 41(19), 6725–6733. <https://doi.org/10.1002/2014GL061507>

862 Rohais, S., & Rouby, D. (2020). Source-to-Sink Analysis of the Plio-Pleistocene Deposits in the Suez  
863 Rift (Egypt). In S. Khomsi, F. M. Roure, M. Al Garni, & A. Amin (Eds.), *Arabian Plate and*  
864 *Surroundings: Geology, Sedimentary Basins and Georesources* (pp. 115–133). Cham:  
865 Springer International Publishing. [https://doi.org/10.1007/978-3-030-21874-4\\_4](https://doi.org/10.1007/978-3-030-21874-4_4)

866 Rohais, S., Barrois, A., Colletta, B., & Moretti, I. (2016). Pre-salt to salt stratigraphic architecture in a  
867 rift basin: insights from a basin-scale study of the Gulf of Suez (Egypt). *Arabian Journal of*  
868 *Geosciences*, 9(4), 317. <https://doi.org/10.1007/s12517-016-2327-8>

869 Simon, B. (2015). *Rift du Lac Albert, Ouganda, Rift Est Africain : déformation, érosion, sédimentation*  
870 *et bilan de matière depuis 17 Ma*. Retrieved from  
871 <http://www.theses.fr/2015REN1S175/document>

872 Sømme, T. O., Skogseid, J., Embry, P., & Løseth, H. (2019). Manifestation of Tectonic and Climatic  
873 Perturbations in Deep-Time Stratigraphy – An Example From the Paleocene Succession  
874 Offshore Western Norway. *Frontiers in Earth Science*, 7, 303.  
875 <https://doi.org/10.3389/feart.2019.00303>

876 Stevens Goddard, A., Carrapa, B., & Aciar, R. H. (2020). Recognizing drainage reorganization in the  
877 stratigraphic record of the Neogene foreland basin of the Central Andes. *Sedimentary*  
878 *Geology*, 405, 105704. <https://doi.org/10.1016/j.sedgeo.2020.105704>

879 Stock, J. D., & Montgomery, D. R. (1999). Geologic constraints on bedrock river incision using the  
880 stream power law. *Journal of Geophysical Research: Solid Earth*, 104(B3), 4983–4993.  
881 <https://doi.org/10.1029/98JB02139>

882 Svartman Dias, A. E., Lavier, L. L., & Hayman, N. W. (2015). Conjugate rifted margins width and  
883 asymmetry: The interplay between lithospheric strength and thermomechanical processes.  
884 *Journal of Geophysical Research: Solid Earth*, 120(12), 8672–8700.  
885 <https://doi.org/10.1002/2015JB012074>

886 Syvitski, J. P. M., & Milliman, J. D. (2007). Geology, Geography, and Humans Battle for Dominance  
887 over the Delivery of Fluvial Sediment to the Coastal Ocean. *The Journal of Geology*, 115(1),  
888 1–19. <https://doi.org/10.1086/509246>

889 Tetreault, J. L., & Buitter, S. J. H. (2018). The influence of extension rate and crustal rheology on the  
890 evolution of passive margins from rifting to break-up. *Tectonophysics*, 746, 155–172.  
891 <https://doi.org/10.1016/j.tecto.2017.08.029>

892 Theunissen, T., & Huismans, R. S. (2019). Long-Term Coupling and Feedback Between Tectonics  
893 and Surface Processes During Non-Volcanic Rifted Margin Formation. *Journal of*  
894 *Geophysical Research: Solid Earth*, 124(11), 12323–12347.  
895 <https://doi.org/10.1029/2018JB017235>

896 Thieulot, C. (2011). FANTOM: Two- and three-dimensional numerical modelling of creeping flows  
897 for the solution of geological problems. *Physics of the Earth and Planetary Interiors*, 188(1–  
898 2), 47–68. <https://doi.org/10.1016/j.pepi.2011.06.011>

899 Walford, H., White, N., & Sydow, J. (2005). Solid sediment load history of the Zambezi Delta. *Earth*  
900 *and Planetary Science Letters*, 238(1–2), 49–63. <https://doi.org/10.1016/j.epsl.2005.07.014>

901 Wang, P., Scherler, D., Liu-Zeng, J., Mey, J., Avouac, J.-P., Zhang, Y., & Shi, D. (2014). Tectonic  
902 control of Yarlung Tsangpo Gorge revealed by a buried canyon in Southern Tibet. *Science*,  
903 346(6212), 978–981. <https://doi.org/10.1126/science.1259041>

904 Whipple, K. X. (2009). The influence of climate on the tectonic evolution of mountain belts. *Nature*  
905 *Geoscience*, 2(2), 97–104. <https://doi.org/10.1038/ngeo413>

906 Whipple, K. X., & Tucker, G. E. (1999). Dynamics of the stream-power river incision model:  
907 Implications for height limits of mountain ranges, landscape response timescales, and research  
908 needs. *Journal of Geophysical Research: Solid Earth*, 104(B8), 17661–17674.  
909 <https://doi.org/10.1029/1999JB900120>

910 Whittaker, A. C. (2012). How do landscapes record tectonics and climate? *Lithosphere*, 4(2), 160–164.  
911 <https://doi.org/10.1130/RF.L003.1>

912 Whittaker, A. C., Attal, M., & Allen, P. A. (2010). Characterising the origin, nature and fate of  
913 sediment exported from catchments perturbed by active tectonics. *Basin Research*, 22(6),  
914 809–828. <https://doi.org/10.1111/j.1365-2117.2009.00447.x>

915 Willett, S. D. (1999). Orogeny and orography: The effects of erosion on the structure of mountain  
916 belts. *Journal of Geophysical Research: Solid Earth*, 104(B12), 28957–28981.  
917 <https://doi.org/10.1029/1999JB900248>

918 Wolf, S. G., Huismans, R. S., Muñoz, J., Curry, M. E., & van der Beek, P. (2021). Growth of  
919 Collisional Orogens From Small and Cold to Large and Hot—Inferences From Geodynamic  
920 Models. *Journal of Geophysical Research: Solid Earth*, 126(2).  
921 <https://doi.org/10.1029/2020JB021168>

922 Yuan, X. P., Braun, J., Guerit, L., Rouby, D., & Cordonnier, G. (2019). A New Efficient Method to  
923 Solve the Stream Power Law Model Taking Into Account Sediment Deposition. *Journal of*  
924 *Geophysical Research: Earth Surface*, 124(6), 1346–1365.  
925 <https://doi.org/10.1029/2018JF004867>

926 Yuan, X. P., Braun, J., Guerit, L., Simon, B., Bovy, B., Rouby, D., et al. (2019). Linking continental  
927 erosion to marine sediment transport and deposition: A new implicit and O(N) method for  
928 inverse analysis. *Earth and Planetary Science Letters*, 524, 115728.  
929 <https://doi.org/10.1016/j.epsl.2019.115728>

930